Nuanced role for dendritic cell intrinsic IRE1 RNase in the regulation of antitumor adaptive immunity

Felipe Flores-Santibañez[1,8,9], Sofie Rennen[2,3,9], Dominique Fernandez[1], Clint De Nolf[2], Sandra Gaete[1], Camila Fuentes[4], Carolina Moreno[1], Diego Figueroa[5], Álvaro Lladser[5,6], Takao Iwawaki[7], María Rosa Bono[8], Sophie Janssens[2,3,*] and Fabiola Osorio[1,*]

[1]Laboratory of Immunology and Cellular Stress, Immunology Program, Institute of Biomedical Sciences, Faculty of Medicine, University of Chile, Av. Independencia 1027, 8380453, Santiago, Chile.
[2]Laboratory for ER Stress and Inflammation, VIB Center for Inflammation Research, Technologiepark, Zwijnaarde 71, B-9052, Ghent, Belgium.
[3]Department of Internal Medicine and Pediatrics, Ghent University, De Pintelaan 185, 9000, Ghent, Belgium.
[4]Laboratory of Cancer Immunoregulation, Immunology Program, Institute of Biomedical Sciences, Faculty of Medicine, University of Chile, Av. Independencia 1027, 8380453, Santiago, Chile.
[5]Laboratory of Immunoncology, Fundación Ciencia & Vida, Av Zañartu 1482, 7780272, Santiago, Chile.
[6]Faculty of Medicine and Science, Universidad San Sebastián, Lota 2465, 7510157 Santiago, Chile.
[7]Division of Cell Medicine, Department of Life Science, Medical Research Institute, Kanazawa Medical University, 1-1 Daigaku, Uchinada, Kahoku, Ishikawa 920-0293 Ishikawa, Japan.
[8]Immunology Laboratory, Biology Department, Faculty of Sciences, University of Chile, Las Palmeras 3425, 7800003, Santiago, Chile.
[9] These authors equally contributed to this work.
* Corresponding authors.

Running title: Nuanced role for DC-intrinsic IRE1 RNase in antitumor immunity

Conflict of interest statement: "The authors have declared that no conflict of interest exists."

Correspondence: Fabiola Osorio
Immunology Program
Institute of Biomedical Sciences
Faculty of Medicine
Universidad de Chile
Av. Independencia 1027
Postal code: 8380453
Santiago
Chile
Phone: +56-2-29789503
Email: fabiolaosorio@med.uchile.cl

Sophie Janssens
Laboratory for Endoplasmic Reticulum Stress and Inflammation
VIB Center for Inflammation Research,
Technologiepark 71
B-9052 Zwijnaarde
Ghent
Belgium
Email: sophie.janssens@irc.vib-ugent.be

ABSTRACT

The IRE1/XBP1s axis of the unfolded protein response (UPR) plays divergent roles in dendritic cell (DC) biology in steady state versus tumor contexts. Whereas tumor associated DCs show dysfunctional IRE1/XBP1s activation that curtails their function, the homeostasis of conventional type 1 DCs (cDC1) in tissues requires intact IRE1 RNase activity. Considering that cDC1s are key orchestrators of antitumor immunity, it is relevant to understand the functional versus dysfunctional roles of IRE1/XBP1s in tumor DC subtypes. Here, we show that cDC1s constitutively activate IRE1 RNase within subcutaneous B16 melanoma and MC38 adenocarcinoma tumor models. Mice lacking XBP1s in DCs display increased melanoma tumor growth, reduced T cell effector responses and accumulation of terminal exhausted $CD8^+$ T cells. Transcriptomic studies revealed that XBP1 deficiency in tumor cDC1s decreased expression of mRNAs encoding XBP1s and regulated IRE1 dependent decay (RIDD) targets. Finally, we find that the dysregulated melanoma growth and impaired T cell immunity noticed in XBP1 deficient mice are attributed to RIDD induction in DCs. This work indicates that IRE1 RNase activity in melanoma/MC38-associated DCs fine tunes aspects of antitumor immunity independently of XBP1s, revealing a differential role for the UPR axis that depends on the DC subtype and cancer model.

Keywords: Dendritic cells, immunity, IRE1, melanoma, unfolded protein response.

107 **ABBREVIATIONS**

108

109 BM: bone marrow

110 cDC: conventional DC

111 cDC1: type 1conventional DC ($XCR1^+$ DC)

112 cDC2: type 2conventional DC ($CD11b^+$ DC)

113 DC: dendritic cell

114 DEG: Differentially expressed gene

115 ER: endoplasmic reticulum

116 ERAI: ER stress-activated indicator

117 Flt3L: FMS-related tyrosine kinase 3 ligand

118 FP: fluorescent protein

119 GSEA: Gene set enrichment analysis

120 IRE1: inositol-requiring enzyme 1 alpha

121 KO: Knock-out

122 MdC: Myeloid derived Cell

123 RIDD: regulated IRE1-dependent decay

124 ROS: reactive oxygen species

125 TAM: tumor-associated macrophages

126 TCR: T cell receptor

127 TdLN: Tumor draining lymph node

128 UPR: unfolded protein response

129 XBP1s: spliced XBP1

130 XBP1u: unspliced XBP1

131

132

133

134

135

136

137 # INTRODUCTION

138 A crucial arm of antitumor immunity relies on effective activation of tumor specific
139 cytotoxic CD8$^+$ T cells endowed with the ability to eliminate cancer cells. This process is
140 critically dependent on type 1 conventional dendritic cells (cDC1), which excel in cross-
141 presentation of tumor-associated antigens (1–3), secrete soluble factors that potentiate
142 CD8$^+$ T cell function (2, 4–7), and prevent the generation of terminal exhausted CD8$^+$ T
143 cells committed to irreversible dysfunctional phenotypes in tumors (8). Tumor cDC1
144 infiltration correlates with improved prognosis (2, 5, 9) and better response to immune
145 checkpoint blockade (ICB) therapy (9–12). Besides, therapeutic strategies
146 expanding/activating tumor cDC1s have shown promising results in clinical trials (11, 13,
147 14). Additional DC subsets such as type 2 DCs (cDC2s), and a novel DC activation state
148 termed 'mregDCs' (mature DCs enriched in immunoregulatory molecules) can also boost
149 antitumor CD4$^+$ and CD8$^+$ T cell responses (7, 15–17), indicating that cDCs are interesting
150 candidates in immunotherapy. However, the molecular mechanisms safeguarding the
151 function of these cells in tumors have not been fully elucidated.

152 An emerging intracellular pathway regulating DC biology is the inositol-requiring enzyme
153 1 alpha (IRE1) branch of the unfolded protein response (UPR), which is an adaptive
154 cellular response maintaining the fidelity of the cellular proteome (18). Upon
155 endoplasmic reticulum (ER) stress, the endoribonuclease (RNase) domain of IRE1 splices
156 *Xbp1* mRNA, generating the transcription factor XBP1 spliced (XBP1s), master regulator
157 of protein folding and ER biogenesis (18–20). The IRE1 RNase domain can also promote
158 the degradation of a subset of mRNAs/miRNAs in a process known as 'regulated IRE1-
159 dependent decay' (RIDD) (21), which is a mechanism beginning to be understood in
160 pathological settings including metabolism, inflammation and cancer (22–24).

161 In steady state, IRE1 regulates cDC homeostasis via constitutive activation of its RNase
162 domain, a feature noticed in cDC1s across several tissues (25, 26). Furthermore, cDC1s
163 are markedly sensitive to perturbations in the IRE1/XBP1s axis, as genetic loss of the
164 transcription factor XBP1 alters proteostatic programs and counter activates the RIDD
165 branch, which mediates the decay of various mRNAs involved in integrin expression, ER
166 to golgi transport and antigen presentation, among others (25, 26). The selectivity of the
167 IRE1/XBP1s axis in cDC1s is underscored in microarray studies of XBP1 deficient cells,
168 which change the transcriptomic landscape of cDC1s but not cDC2s (26). As such, cDC1s
169 opt the IRE1/XBP1s axis for proper function in steady state, but it is unclear if the pathway
170 displays similar roles in cDC1s infiltrating tumors. This is a relevant question, as reported
171 work shows that metabolically stressed tumors elicit maladaptive UPR activation in
172 certain tumor immune cells (including DCs), which reprograms their phenotype towards
173 dysfunctional states that promote tumor growth (27, 28). For instance, DCs infiltrating
174 ovarian cancer (typified by expression of the cDC2/monocyte marker CD11b^{+} (29))
175 display persistent IRE1/XBP1s activation that triggers aberrant intracellular lipid
176 accumulation, resulting in impaired immunostimulatory functions and leading to tumor
177 progression (30). Thus, these data suggest that IRE1 may play different, or even opposite
178 roles in DC biology depending on the subtype or the inflammatory context. As such, a
179 correct delineation of the role of the enzyme in tumor cDCs is required to understand if
180 intervention of this UPR branch can be targeted for potential cancer therapies.
181 In this work, we study the role of IRE1/XBP1s in DCs by focusing on two
182 immunoresponsive tumor models: subcutaneous mouse B16/B78 melanoma and MC38
183 colon adenocarcinoma (2, 10). We identified that cDC1s display constitutive IRE1 RNase
184 activity in tumors, which follows a lineage-intrinsic trait not influenced by the tumor
185 microenvironment. In contrast to previous reports (30), deletion of XBP1 in DCs did not

186 decrease tumor burden. Rather, XBP1 deficiency in DCs resulted in a moderate increase
187 of tumor growth, lower frequencies of intratumoral effector T cells, and accumulation of
188 terminal exhausted TIM-3^{+}CD8^{+} cells in the melanoma model. Transcriptomic studies
189 revealed that XBP1 deficient tumor cDC1s downregulate proteostatic processes and
190 decrease the expression of mRNAs encoding XBP1s and regulated IRE1 dependent decay
191 (RIDD) targets. Importantly, animals bearing double deletion of IRE1 RNase and XBP1 in
192 DCs display normal tumor growth and adaptive immunity in the melanoma model,
193 highlighting a role for IRE1 RNase hyperactivation in fine tuning aspects of antitumor
194 immunity via DCs.
195
196
197
198
199
200
201
202
203
204
205
206
207
208
209
210

211 # RESULTS

212 **cDC1s constitutively activate IRE1 RNase in subcutaneous melanoma and MC38**
213 **colon carcinoma tumors**

214 The tumor microenvironment contain activators of the IRE1/XBP1s axis that are detected
215 by immune cells (27, 30–32). To identify relevant cell types activating IRE1 RNase in
216 tumors, we analyzed the immune composition of B16 tumors of ERAI mice, a mouse strain
217 that reports IRE1 RNase activity through expression of Venus Fluorescent Protein
218 (VenusFP) fused with the sequence of *Xbp1s* mRNA (33) (validated in (25, 26, 31)). To
219 allow unsupervised identification of IRE1 RNase cellular targets, we devised a 17-color
220 flow cytometry panel and data was visualized on a *t*-distributed stochastic neighbor
221 embedding (*t*-SNE) map. Cells were grouped into populations by DBScan-guided
222 automated clustering (Fig. 1A-B, Supp. Fig. 1A), which identified 15 cell clusters that
223 included $CD8^+$ T cells, $CD4^+$ T cells, monocyte-derived cells (MdCs), MHC-II-expressing
224 MdCs, NK cells, NKT cells, B cells, neutrophils and cDC1s. As expected (17), cDC2s and
225 tumor associated macrophages (TAMs) (clusters 4 and 6) showed a degree of
226 heterogeneity and convergence. Also, our analysis revealed two undefined clusters based
227 on surface marker expression; Cluster 11: $CD4^+$ $CD11c^+$ $CD26^+$, and Cluster 14: $CD3^+$ $CD4^+$
228 $CD11b^{int}$ $F4/80^+$ MHC-II^{high} $CD11c^{int}$ $CD26^{high}$.

229 Next, IRE1 RNase activity from the ERAI reporter mice line was determined in the clusters
230 of the t-SNE plot (Fig. 1C-D). Data indicated that among $CD45^+$ hematopoietic cells, cDC1s
231 represented the population with highest fluorescence intensity of VenusFP (Fig 1C-D,
232 cluster 15). Additional immune cells including cDC2s, MdC, MHC-II^+MdC, TAM,
233 neutrophils, NK cells and cells from cluster 11 also showed noticeable VenusFP induction,
234 albeit at lower levels than cDC1s; whereas $CD4^+$ T cells, $CD8^+$ T cells and B cells showed
235 little or no induction of VenusFP compared to cells from control animals (Fig 1D). Manual

236 gating analysis (Fig. 1E-F, Supp. Fig. 2A) confirmed that the mean fluorescence intensity
237 (MFI) of VenusFP in melanoma-associated cDC1s was higher than additional myeloid and
238 lymphoid cells (Fig. 1E-F). Notably, similar results were observed in cDC1s infiltrating
239 MC38 tumors (Supp. Fig. 1B). Finally, these data was confirmed by PCR for endogenous
240 *Xbp1* spliced and unspliced forms from tumor cDC1s isolated from wild type (WT)
241 animals implanted with the B16-FLT3L melanoma cell line (which expresses the DC-
242 differentiation factor FMS-like tyrosine kinase 3 ligand (FLT3L) (11, 34)). Data in Fig. 1G-
243 H showed that tumor cDC1s expressed marked levels of *Xbp1s*, which was even superior
244 to the levels noticed in bone-marrow derived DCs (BMDC) stimulated with the
245 pharmacological UPR inducer tunicamycin. Altogether, these data indicate that cDC1s
246 display prominent activation of the IRE1/XBP1s axis in tumors.
247 We next interrogated whether the augmented IRE1 RNase activity observed in tumor
248 cDC1s is a lineage-intrinsic signature or if it is a feature imposed by the tumor
249 microenvironment. We quantified the VenusFP MFI of cDC1s directly exposed to the
250 tumor (tumor cDC1 and migratory cDC1s of the tumor draining lymph node (TdLN)),
251 versus TdLN resident cDC1s, which do not access to the tumor site (gating strategy in
252 Supp. Fig. 2B) (35). Data depicted in Fig. 1I indicates that tumor cDC1s express lower
253 levels of VenusFP than resident cDC1s, indicating that tumor exposure does not increase
254 IRE1 RNase activity in these cells. Similar observations were made for cDC2s (Fig 1I). In
255 fact, cDC1s infiltrating MC38 tumors express markedly lower levels of VenusFP than
256 spleen cDC1s (Supp. Fig. 1C). Of note, this observation was not replicated in monocytes,
257 which express higher VenusFP levels in the tumor compared to the spleen (Fig 1J).
258 Altogether, these data suggest that IRE1 RNase activation in tumor cDCs is a stable lineage
259 intrinsic trait not driven by the microenvironment.
260

261 **XBP1 deletion in CD11c-expressing cells results in increased melanoma tumor**
262 **growth**

263 To gain insights on the role of XBP1 in DCs during melanoma tumor growth, we studied
264 the *Itgax*-Cre x *Xbp1*$^{fl/fl}$ mice (36, 37), referred to as 'XBP1$^{\Delta DC}$' mice, in which exon 2 of
265 *Xbp1* is excised in CD11c-expressing cells, resulting in absence of the transcription factor
266 in DCs (26). These animals were compared to control littermates (*Xbp1*$^{fl/fl}$ animals with
267 no expression of Cre), referred to as 'XBP1^{WT}' mice. XBP1^{WT} and XBP1$^{\Delta DC}$ mice were
268 implanted with the B78-ChOVA melanoma line, a B16 variant that expresses the
269 ovalbumin (OVA) antigen and mCherry fluorescent protein (2). Data in Figure 2A-B
270 indicate that XBP1$^{\Delta DC}$ mice showed moderate but noticeable acceleration of tumor growth
271 and significantly larger tumor size than tumors from XBP1^{WT} mice on day 12 post
272 implantation (80.44 ± 8.927 vs 56.56 ± 6.174 mm^3, p = 0.0312, mean ± s.e.m.) (Fig. 2B).
273 As a second tumor model, we also analyzed growth of subcutaneous MC38 murine colon
274 adenocarcinoma tumors, which also showed a trend towards increased tumor growth in
275 XBP1$^{\Delta DC}$ mice, but without reaching statistical significance (Supp. Fig. 3A-C).

276 To understand if XBP1 deficiency in the CD11c compartment resulted in altered cell
277 recruitment, we quantified the immune cell composition at the melanoma tumor site.
278 XBP1^{WT} and XBP1$^{\Delta DC}$ mice show similar numbers of CD45$^+$ cells (Fig. 2C), and comparable
279 composition of tumor cDC1/cDC2 and resident and migratory cDC1/cDC2s in the TdLN
280 (Fig. 2D-E). Furthermore, conditional *knock-out* and control animals also showed
281 comparable frequencies of myeloid and lymphoid cells (Fig. 2F-H). These data indicate
282 that XBP1s expression by DCs infiltrating melanoma and MC38 tumor does not promote
283 tumor progression. Rather, loss of XBP1s in DCs leads to increased melanoma tumor
284 growth by mechanisms that are independent of immune cell recruitment.
285

286 **XBP1 deletion in CD11c-expressing cells results in impaired antitumor T cell**
287 **responses and disbalanced precursor/terminal exhausted T cell ratio**

288 We next focused our analysis on DC function. It was recently identified a conserved
289 immunoregulatory transcriptional program activated by tumor DCs based on the co-
290 expression of the molecules CD40 and PDL-1 plus the cytokine IL-12 (15). Our analysis
291 revealed that tumor and migratory cDC1/cDC2s from XBP1$^{\Delta DC}$ mice express normal levels
292 of these molecules (Fig. 3A, Supp. Fig. 4A). We also studied bone marrow cDC1s generated
293 upon culture with OP9-DL1 stromal cell line plus FLT3L (reported in (38, 39)). We found
294 that bone marrow cDC1s from XBP1$^{\Delta DC}$ mice produce lower levels of IL-12 in
295 unstimulated conditions (Fig 3B, Supp. Fig. 4B). However, upon tumor exposure,
296 expression of IL-12 was comparable between XBP1 sufficient and deficient cDC1s. We
297 conclude that XBP1s regulate certain parameters of DC activation in steady state that are
298 restored upon tumor encounter.

299 Considering previous findings showing that XBP1s deficient cDC1s have impaired cross-
300 presentation abilities in steady state (26), we interrogated if the mice line was able to
301 cross-present melanoma-associated antigens. We implanted B78ChOVA tumors in
302 XBP1^{WT} and XBP1$^{\Delta DC}$ mice and quantified the presence of endogenous OVA-specific CD8^{+}
303 T cells using H-2K^{b}-OVA$_{257-264}$ tetramers. XBP1^{WT} and XBP1$^{\Delta DC}$ contained similar
304 frequencies of OVA-specific CD8^{+} T cells in tumors and TdLN (Fig. 3C-D, Supp. Fig 4C). A
305 similar response was obtained when tracking proliferation/early activation of CD8^{+} T
306 cells isolated from pmel mice, which possess transgenic CD8^{+} T cells bearing a TCR
307 selective for the melanoma-associated antigen gp100 (40) (Supp. Fig. 4D-E). Thus, we
308 conclude that XBP1 deletion in tumor-associated CD11c^{+} cells does not prevent cross-
309 presentation of melanoma-associated antigens.

310 We next investigated the quality of the antitumor T cell response evoked in XBP1$^{\Delta DC}$ mice.
311 As a measure of T cell quality, we analyzed cytokine producing T cells from tumors of
312 XBP1^{WT} and XBP1$^{\Delta DC}$ mice. Tumors from XBP1$^{\Delta DC}$ mice contained lower frequencies of
313 IFN-γ-producing and TNF-producing CD8$^+$ T cells, which also resulted in decreased
314 frequencies of double producers IFN-γ$^+$TNF$^+$ CD8$^+$ T cells and triple producers IFN-
315 γ$^+$TNF$^+$IL-2$^+$ CD8$^+$ T cells (Fig. 3E-F). These observations were also noticed in the CD4$^+$ T
316 cell compartment, as reduced frequencies of IFN-γ$^+$ CD4$^+$ T cells and IFN-γ$^+$ TNF$^+$ CD4$^+$ T
317 cells were found in tumors from XBP1$^{\Delta DC}$ mice (Fig. 3G). As such, absence of XBP1 in
318 CD11c-expressing cells results in decreased CD8$^+$ and CD4$^+$ T cell effector function in
319 melanoma tumors. Analysis of the MC38 model showed that whereas the CD8$^+$ T cell
320 response was not affected, there was a significant reduction in the frequencies of IFN-γ-
321 producing and IFN-γ/ TNF-producing CD4$^+$ T cells (Supp. Fig. 4F-G).
322 Impaired cytokine production is a hallmark of CD8$^+$ T cell exhaustion in cancer (41, 42),
323 a process characterized by a progressive loss of function that culminates with the
324 generation of terminal exhausted TIM-3$^+$CD8$^+$ T cells unable to control tumor growth
325 (42). TIM-3$^+$CD8$^+$ T cells do not proliferate, are unresponsive to anti-PD1 therapy (41, 43)
326 and originate from 'precursor exhausted' CD8$^+$ T cells, a T cell state characterized by the
327 expression of the transcription factor TCF-1 (termed 'TCF1$^+$CD8$^+$ T cells'), which retain
328 proliferative potential and can be reinvigorated through anti-PD1 therapy (41, 43, 44).
329 We determined the presence of intratumoral TCF-1$^+$CD8$^+$ T cells and TIM-3$^+$CD8$^+$ T cells
330 in melanoma tumors from XBP1$^{\Delta DC}$ mice and control animals. Tumors from XBP1$^{\Delta DC}$ mice
331 show decreased infiltration of TCF-1$^+$CD8$^+$ T cells and increased proportions of TIM-
332 3$^+$CD8$^+$ T cells compared to tumors from control animals (Figure 3H-I). Additionally,
333 TIM3$^+$ CD8$^+$ T cells from XBP1^{WT} and XBP1$^{\Delta DC}$ mice display a *bona-fide* terminal exhausted
334 phenotype, with elevated levels of CD39, TOX and granzyme B (Supp. Fig. 4H). These

335 findings are consistent with data depicted in figure 3E-F showing lower frequencies of
336 polyfunctional cytokine-producing $CD8^+$ T cells in tumors from $XBP1^{\Delta DC}$ mice, which is an
337 attribute of precursor exhausted $TCF\text{-}1^+CD8^+$ T cells (41). Altogether, our data shows that
338 XBP1s in the $CD11c^+$ compartment coordinates the balance of $CD8^+$ T cell profiles in
339 melanoma.
340

341 **Tumor cDC1s from $XBP1^{\Delta DC}$ mice display signs of RIDD**

342 Thus far, our data indicate that XBP1s expression in DCs modulates melanoma tumor
343 growth and the balance of effector and exhausted T cell subsets. However, it is unclear if
344 these processes depend on XBP1s-transcriptional activity, as previous work
345 demonstrated that XBP1s deficiency leads to hyperactivation of IRE1 RNase and RIDD in
346 steady state cDC1s (25, 26). Thus, we interrogated if XBP1 deficiency also resulted in
347 increased IRE1 RNase activity in tumor cDC1s (Fig 4A). We measured expression of *Xbp1*
348 spliced/unspliced mRNA in tumor cDC1s from control and $XBP1^{\Delta DC}$ mice. Although
349 $XBP1^{\Delta DC}$ cDC1s are unable to synthesize XBP1s protein, these cells still generate *Xbp1*
350 mRNA bearing the IRE1 cleavage sites, which serves as an assay to monitor IRE1 RNase
351 activity (26). Data in Figure 4B show that tumor cDC1s isolated from $XBP1^{\Delta DC}$ mice
352 express marked levels of *Xbp1s* mRNA compared to control counterparts, which is an
353 indicative sign of IRE1 RNase hyperactivation.
354 To determine RIDD on protein level in tumor DCs, we determined surface expression of
355 the integrin CD11c, a dimeric partner of *Itgb2* (coding the integrin CD18), which is a
356 reported mRNA substrate of IRE1 RNase (26). CD11c surface expression depends on
357 RIDD-mediated degradation of *Itgb2* mRNA and therefore, it can be used as a surrogate
358 marker for RIDD activity. Data in Fig. 4C show that tumor cDC1s from $XBP1^{\Delta DC}$ express
359 lower surface levels of CD11c than control counterparts, confirming RIDD induction on

360 protein level. Similar effect was observed in cDC1 subsets from the TdLN (Fig 4D). These
361 data show that XBP1-deficient cDC1s display signs of RIDD in melanoma tumors.
362 Interestingly, additional APCs such as tumor cDC2s and TAM from XBP1$^{\Delta DC}$ mice showed
363 a modest but noticeable reduction in CD11c expression (Fig. 4C), suggesting that these
364 cells may also induce RIDD upon XBP1 loss, albeit at lower extent than cDC1s.
365
366 **Gene expression profiles of tumor cDC1s deficient for IRE1 RNase and XBP1**
367 Given that XBP1 deficient cDC1s show signs of RIDD at the tumor site, we analyzed the
368 transcriptomic signature downstream of IRE1 RNase in melanoma-infiltrating cDC1s. To
369 identify specific XBP1-dependent and RIDD-dependent targets, we carried out a parallel
370 analysis of the transcriptome of tumor cDC1s deficient for XBP1, or double deficient for
371 the RNase domain of IRE1 and XBP1. To generate double *knock-out* animals for the IRE1
372 RNase and XBP1 in CD11c-expressing cells, we crossed XBP1$^{\Delta DC}$ mice with *Ern1*$^{fl/fl}$ mice,
373 which bear loxP sites flanking exon 20 and 21 of the *Ern1* gene and generates a truncated
374 IRE1 isoform lacking the RNase domain (45) (referred to as "XBP1$^{\Delta DC}$/IRE1^{trunc}DC mice").
375 As such, XBP1$^{\Delta DC}$ mice lack the transcription factor and activate RIDD, whereas double
376 deficient XBP1$^{\Delta DC}$/IRE1^{trunc}DC mice lack both XBP1s and RIDD (Supp. Fig 5A-C). With this
377 strategy, XBP1s target genes are identified as transcripts that are downregulated in tumor
378 cDC1s from both XBP1$^{\Delta DC}$ and XBP1$^{\Delta DC}$/IRE1^{trunc}DC mice. In contrast, RIDD-dependent
379 transcripts are recognized as mRNAs that decrease their expression in XBP1-deficient
380 tumor cDC1s, but which expression is restored in XBP1$^{\Delta DC}$/IRE1^{trunc}DC animals.
381 Tumor cDC1s were isolated by cell sorting from B16 melanoma tumors of control,
382 XBP1$^{\Delta DC}$ or XBP1$^{\Delta DC}$/IRE1^{trunc}DC mice and the transcriptome was analyzed by bulk RNA
383 sequencing (RNA-seq). 51 differentially expressed genes (DEG) were identified among
384 XBP1$^{\Delta DC}$ or XBP1$^{\Delta DC}$/IRE1^{trunc}DC cDC1s (adjusted p-value < 0.05 and $|\text{Fold Change}| > 1.5$)

385 (Fig. 5A). Biological pathway enrichment analysis using Gene Ontology (GO)
386 knowledgebase revealed that a large proportion of DEGs are constituents of the response
387 to misfolded proteins and transport and localization of ER proteins (see Biological
388 Process, Fig. 5B). There was also an overrepresentation of protein disulfide-isomerases
389 (see Molecular Function, Fig. 5B) and on intracellular localization level, most deregulated
390 genes encoded ER proteins (see Cellular Component, Fig. 5B). Next, we analyzed the DEGs
391 per mice line, which clustered these genes into three main groups: (1) genes upregulated
392 in XBP1-deficient and IRE1 RNase/XBP1-deficient tumor cDC1s; (2) genes
393 downregulated in both XBP1-deficient and IRE1 RNase/XBP1-deficient tumor cDC1s
394 (XBP1s targets); and (3) genes downregulated exclusively in XBP1-deficient tumor cDC1s
395 (potential RIDD targets) (Fig. 5A). In group (1), we identified five transcripts including
396 *Hspa5* which encodes BiP, a chaperone induced upon UPR activation (46). This finding
397 indicates that XBP1-deficient and IRE1 RNase/XBP1-double deficient tumor cDC1s show
398 signs of ER stress (Fig. 5A). We also identified *Cox6a2* (subunit of cytochrome C oxidase),
399 which was previously identified as an upregulated gene in XBP1-deficient cDC1s (26).
400 Transcripts in group (2) include protein disulfide isomerases (*Erp44, Txndx11, Txndc5,*
401 *P4hb*) chaperones (*Dnajb9/Hyou1*); glycosylation proteins (*Rpn1, Alg2, Serp1*), proteins
402 involved in transport to the ER (*Sec61a1, Sec61b, Spcs2, Spcs3, Ssr3*) and from the ER to
403 Golgi (*Bet1, Surf4*) (Fig. 5A). Additional canonical XBP1s targets (*Stt3a* and *Edem2)* were
404 identified when the cut off value was set below 1.5-fold (Supp. Fig 6A). Gene Set
405 Enrichment Analysis (GSEA) revealed that the transcriptome of both XBP1$^{\Delta DC}$ and
406 XBP1$^{\Delta DC}$/IRE1^{trunc}DC tumor cDC1s were depleted of targets related to protein
407 glycosylation, ER to Golgi transport, protein localization to the ER and lipid biosynthesis
408 (Fig 5C-D).

409 Finally, group (3) includes the canonical RIDD substrates *Bloc1s1*, *St3gal5* (21), *Itgb2* (26),
410 plus a subset of transcripts with heterogeneous functions (Fig. 5A) that range from lipid
411 synthesis and metabolism members (*St3gal5, Gm2a, Abca2*), Ca^{+2} homeostasis (*Stim2,*
412 *Pkd1*), protein folding (*Qsox1, Mlec*), a steroid binding receptor (*Paqr7*), an amino acid
413 transporter (*Slc1a5*) , a member of the nuclear pore complex (*Nup210*), an E3-ubiquitin
414 ligase (*Rnf130*), signaling receptors in immunity and development (*Fcrla*, *Notch4*,
415 respectively) to *Eif2ak3,* which encodes the UPR transducer PERK. Consistent with the
416 functional heterogeneity of RIDD targets, GSEA did not reveal differences at the level of
417 biological processes between XBP1$^{\Delta DC}$ and XBP1$^{\Delta DC}$/IRE1^{trunc}DC cDC1s (Fig 5C-D). Even
418 though some processes such as antigen processing and presentation and cell-redox
419 homeostasis are downregulated exclusively in tumor cDC1s from XBP1$^{\Delta DC}$ mice (thereby
420 suggesting RIDD dependency), these processes display low enrichment scores. To sum
421 up, these data indicate that tumor cDC1s from XBP1$^{\Delta DC}$ mice display an altered XBP1s
422 transcriptional program related to protein homeostasis and folding, and counter activate
423 RIDD. Using GSEA and reported XBP1s-target and RIDD-target gene datasets (31, 47) we
424 confirmed downregulation of the canonical XBP1s transcription program in both XBP1$^{\Delta DC}$
425 cDC1s and double deficient XBP1$^{\Delta DC}$/IRE1^{trunc}DC cDC1s (Fig 5E-F, Supp. Fig. S6B),
426 whereas RIDD-dependent targets are predominantly downregulated in XBP1$^{\Delta DC}$ cDC1s
427 (Fig 5E-F, Supp Fig. S6B). Finally, our findings reveal that melanoma-infiltrating cDC1s do
428 not show signs of dysfunctional XBP1s activity, as genes related to triglyceride
429 biosynthesis that are associated with diminished DC function in other cancer settings are
430 not downregulated upon XBP1s or IRE1 RNase loss (Supp. Fig. 6C-D) (30). Taken together,
431 these results demonstrate that XBP1 deficiency in tumor cDC1s impairs transcriptomic
432 programs associated with the maintenance of proteostasis and induces RIDD.
433

434 **RIDD activation in DCs accounts for the changes related to tumor growth and**
435 **dysregulated antitumor T cell immunity noticed in XBP1$^{\Delta DC}$ mice**

436 Our observations raise the question as to whether the increased tumor growth and T cell
437 dysregulation noticed in XBP1$^{\Delta DC}$ mice is due to XBP1s- or RIDD-dependent outputs in
438 DCs. To address this issue, we implanted the B78ChOVA cell line in control and
439 XBP1$^{\Delta DC}$/IRE1^{trunc}DC animals (Fig. 6A-B), in which RIDD is abolished (Supp. Fig. 5A-C).
440 Remarkably, in contrast to the observations noticed in XBP1$^{\Delta DC}$ mice (Fig. 2A), the tumor
441 size of animals lacking both XBP1 and IRE1 RNase in DCs was comparable to that
442 observed in control animals (41.78 ± 9.033 vs 53.90 ± 12.36 mm^3, p=0.42, mean ± s.e.m.)
443 (Fig. 6B), indicating that RIDD activation in CD11c-expressing cells accounts for the
444 increased tumor growth. Furthermore, we examined whether the reduced frequencies of
445 cytokine producing CD8$^+$ T cells and the disbalance between TCF-1$^+$/TIM-3$^+$ CD8$^+$ T cells
446 noticed in XBP1$^{\Delta DC}$ mice are also dependent on RIDD. Analysis of tumor-infiltrating CD8$^+$
447 T cells revealed no differences in the frequencies of IFN-γ producing CD8$^+$T cells, TNF
448 producing CD8$^+$T cells, IL-2 producing CD8$^+$T cells, nor in the proportion of double or
449 triple cytokine producers between XBP1$^{\Delta DC}$/IRE1^{trunc}DC mice and control animals (Fig.
450 6C-D). Similar results were observed for IFN-γ producing or double IFN-γ/ TNF-α
451 producing CD4$^+$ T cells (Fig. 6E). In addition, analysis of the composition of precursor-
452 exhausted/terminal exhausted T cells revealed similar infiltration of TCF-1$^+$/TIM-3$^+$ CD8$^+$
453 T cells in melanoma tumors from XBP1$^{\Delta DC}$/IRE1^{trunc}DC mice versus control animals (Fig.
454 6F-G), indicating that IRE1 RNase activity in DCs accounted for the accumulation of
455 dysfunctional CD8$^+$ T cells in melanoma. Altogether, these data indicates that
456 hyperactivation of the RNase domain of IRE1 in DCs fine tunes melanoma tumor growth
457 and antitumor T cell immunity.

458

459 # DISCUSSION

460 The IRE1/XBP1s axis has emerged as a critical regulator of immunity and cancer (27, 48,
461 49). The differential mechanisms by which IRE1 signaling integrates the intensity and
462 duration of ER stress to regulate cell fate is particularly noticed in the immune system,
463 with cells such as cDC1s, B cells, NK cells and eosinophils that opt for an intact
464 IRE1/XBP1s axis to maintain cellular health (25, 31, 50, 51), or cells including TAM/MdCs
465 or intratumoral T cells, which acquire dysfunctional phenotypes upon enforced activation
466 of the UPR sensor (27, 32, 52).

467 Here, we report that loss of XBP1 in CD11c-expressing cells results in increased
468 melanoma tumor growth, decreased frequencies of cytokine-producing T cells and
469 accumulation of terminal exhausted TIM-3^{+}CD8^{+} T cells. Notably, this effect is abrogated
470 in XBP1$^{\Delta DC}$/IRE1^{trunc}DC mice, demonstrating that IRE1 RNase-dependent, XBP1s-
471 independent outputs account for the dysregulated antitumor immunity in melanoma. We
472 also observe a milder phenotype in the MC38 model, suggesting that different tumor
473 models differentially regulate the IRE1/XBP1s axis in DCs.

474 The results presented in this work contrast with previous studies demonstrating that
475 persistent IRE1/XBP1s activation in tumor DCs curtails their antitumor function. In
476 ovarian cancer, the same XBP1$^{\Delta DC}$ mice line show marked inhibition of tumor progression
477 and improved antitumor immunity (30). One possibility accounting for these differences
478 may be related to the different composition of DCs infiltrating these cancer models. In
479 ovarian cancer models, tumor-associated DCs are spontaneously immunosuppressive
480 (53) and in fact, whereas depletion of CD11c^{+} cells delays ovarian cancer progression in
481 later stages (54), the same process curtails CD8^{+} T cell priming in melanoma (55).
482 Furthermore, XBP1 deficiency in ovarian cancer DCs does not lead to RIDD activation
483 (30), which contrasts to the evidence presented in this work. Thus, as result of these

484 combined data, we must consider that the outcome of the IRE1 outputs in tumor DCs may
485 drastically differ depending on the DC subset and the cancer type. In fact, data presented
486 here show that animals lacking both XBP1 and IRE1 RNase in DCs display normal
487 melanoma tumor growth and T cell immunity, indicating that the deletion of an entire
488 branch of the UPR in DCs does not have a predetermined role across different tumor types.
489 These results complement existing literature and may be relevant for building a
490 comprehensive understanding on future manipulation of the IRE1/XBP1s axis in cancer.
491 In addition, even though we use a genetic model of XBP1 deletion to reveal the scope of
492 RIDD in tumor DCs which may not recapitulate physiological responses, our work alludes
493 to cDC1s as regulators of anti-melanoma T cell immunity in XBP1$^{\Delta DC}$ mice. First, cDC1s are
494 the subset with the highest IRE1 RNase activity within melanoma and MC38 tumor niches,
495 and T cell parameters altered by XBP1 loss in CD11c^{+} cells, such as the induction of
496 intratumoral IFN-γ producing CD8^{+} T cells and the maintenance of precursor exhausted
497 TCF1^{+}CD8^{+} T cells are attributed to cDC1 function (8, 11). Furthermore, these processes
498 are also dependent on RIDD activation by DCs, which is more strongly induced in cDC1s
499 from XBP1$^{\Delta DC}$ mice (25, 26). Nevertheless, as we also observe reduced frequencies of
500 tumor infiltrating CD4^{+} IFNγ^{+} T cells in XBP1$^{\Delta DC}$ mice in melanoma and MC38 models, a
501 contribution of IRE1 RNase in CD4^{+} T cell priming by tumor cDC1s (56) or also by cDC2s
502 (17) cannot be excluded.
503 On a mechanistic level, we do not find a role for IRE1 RNase in cross-presentation of tumor
504 antigens, contrasting with previous findings in steady state cDC1s (26). These data
505 suggest that tumors may shape the spectra of XBP1s/RIDD targets in infiltrating cDC1s or
506 that additional mechanisms (or DC subtypes) may compensate for the process. In fact,
507 *tapbp* mRNA, a previously identified RIDD target in XBP1-deficient splenic DCs
508 contributing to antigen cross-presentation is not found as DEG in the transcriptomic

509 analysis of this study. In addition, growing evidence demonstrating the capacity of tumor
510 DCs to carry out cross-dressing of MHC-I/peptide complexes from tumor cells adds a new
511 layer of complexity that remains to be addressed (57, 58). However, one novel candidate
512 identified in this analysis as a potential RIDD substrate, the ER-resident FC receptor Like
513 A (*Fcrla)* (Fig. 5A), has been previously identified as part of a BATF3/IRF8 transcriptional
514 program that confers tumor immunogenicity in cDC1s independently of cross-
515 presentation (59). As such, data presented here delineates for first time the XBP1s-
516 dependent and RIDD-dependent targets in tumor cDC1s, which may serve as basis for
517 future studies focused on addressing the role of selective IRE1 RNase targets involved in
518 the regulation of antitumor immunity.
519 Multiple efforts are currently focused on the development of pharmacological compounds
520 targeting the IRE1 RNase active site and XBP1s *in vivo*, many of which have shown
521 translational potential in cancer (60). A recent study revealed that RIDD regulates
522 expression of the MHC-I heavy chain mRNAs in DCs and that inhibition of IRE1 RNase
523 through systemic administration of small molecules greatly attenuates tumor growth in
524 4T1 and CT26 models, by a mechanism proposed to be dependent on DC cross-
525 presentation (61). Even though we do not find MHC-I heavy chain mRNAs as DEGs in the
526 transcriptomic analysis of tumor cDC1s from XBP1$^{\Delta DC}$/IRE1^{trunc}DC mice, and we do not
527 find an improved melanoma tumor response in XBP1$^{\Delta DC}$/IRE1^{trunc}DC animals, future
528 studies are required to integrate these findings through experiments that include kinetics
529 of comparable tumor models. Finally, the work presented here serves as a proof-of-
530 concept study demonstrating that IRE1 RNase dependent, XBP1s-independent outputs in
531 DCs may also contribute to fine-tuning antitumor immunity.
532
533

534 # MATERIAL AND METHODS

535 **RESOURCE AVAILABILITY**

536 Further information and requests for resources and reagents should be directed to
537 Fabiola Osorio (fabiolaosorio@med.uchile.cl).

538

539 ***Materials availability***

540 This study did not generate new unique reagents.

541

542 ***Data and code availability***

543 RNA-seq data have been deposited at GEO and are publicly available as of the date of
544 publication. Accession numbers are listed in supplementary resources table. This paper
545 does not report original code. Any additional information required to reanalyze the data
546 reported in this paper is available upon request.

547

548 **EXPERIMENTAL MODEL AND SUBJECT DETAILS**

549 ***Mice***

550 ERAI (33), XBP1^{WT}(XBP1fl/fl (36)), XBP1$^{\Delta DC}$ (XBP1fl/fl x CD11c-Cre (37)),
551 XBP1^{WT}/IRE1^{WT} (XBP1fl/fl x IRE1fl/fl (45)), XBP1$^{\Delta DC}$ IRE1^{trunc}DC (XBP1fl/fl x IRE1fl/fl x
552 CD11c-Cre) mice were bred at Universidad de Chile and Fundación Ciencia y Vida in
553 specific pathogen-free conditions. Also, for RNA seq studies XBP1^{WT}, XBP1$^{\Delta DC}$,
554 XBP1^{WT}/IRE1^{WT} and XBP1$^{\Delta DC}$ IRE1^{trunc}DC mice were bred at the animal facility at VIB
555 institute. pmel-1 mice (40) were kindly donated by Dr F. Salazar-Onfray. All mice were
556 kept on a C57BL/6 background. Litters with mice of both sexes at 6–14 weeks of age were
557 used for experiments.

558

559 ***Cell Lines***

560 B78-ChOVA cells were kindly provided by Dr. Matthew Krummel (UCSF) (2). B16-F10
561 cells were obtained from ATCG (#CRL-6475). B16-FLT3L cell line (62) was provided by
562 Dr. Maria Rosa Bono (University of Chile). MC-38 cell line was provided by Dr. Álvaro
563 Lladser (Universidad San Sebastian). OP9 cells expressing Notch ligand DL1 (OP9-DL1)
564 (63) were kindly provided by Dr. Juan Carlos Zuñiga-Pflucker (Sunnybrook Research
565 Institute, Canada). Cells were cultured under standard conditions prior to injection into
566 mice. Briefly, cells were cultured in DMEM (B78-ChOVA) or RPMI-1640 (B16-F10/B16-
567 FLT3L/MC-38) supplemented with 10% v/v inactivated fetal bovine serum (FBS, Gibco),
568 100 U/mL penicillin (Corning), 100 μg/mL streptomycin (Corning) and 0.55 mM 2-
569 Mercaptoethanol (Gibco). For MC-38 culture, media was supplemented additionally with
570 non-essential amino acids (ThermoFisher Scientific) and 1 mM sodium pyruvate
571 (ThermoFisher Scientific). Cells were cultured on T75 tissue-culture treated plastic flasks
572 at 37°C, 5% CO_2. Cells were split every other day. OP-DL1 cells were cultured in MEM-
573 alpha medium supplemented with 20% FBS (Gibco), 100 U/mL penicillin (Corning), 100
574 μg/mL streptomycin (Corning), 1mM sodium pyruvate (brand) and 0.55 mM 2-
575 Mercaptoethanol (Gibco).

576

577 **METHOD DETAILS**

578 ***Tumor Model***

579 Tumor cell lines were harvested, washed with PBS, and resuspended in a final injection
580 volume of 50 μl PBS. $5x10^5$ (B16/B78-ChOVA) or $1x10^6$ (MC-38) tumor cells were injected
581 in the right flank of shaved mice intradermally and allowed to grow for 10-15 days. For

582 tumor growth curves, tumor size was determined by two orthogonal measurements with
583 a caliper and the volume was estimated as (width^2 x length)/2.
584
585 ***Preparation of Cell Suspensions***
586 Tumors were minced and digested with Collagenase D (1 mg/mL, Roche) and DNAse I (50
587 µg/mL, Roche) for 30 minutes at 37°C in a water bath. Digested tissue was then passed
588 through a 70 µm cell strainer, followed by red blood cell lysis with RBC lysis buffer
589 (Biolegend). Single cells were kept on ice.
590 For whole intratumoral immune cell profiling and DC stainings, CD45-biotin magnetic
591 positive selection (MACS, Miltenyi) was performed to enrich for total tumor immune
592 infiltrate.
593 For intratumoral T cell stainings, hematopoietic cells were enriched by density gradient
594 centrifugation with 40/70 Percoll (GE Healthcare) for 20 min at 700xg.
595 Tumor draining lymph nodes (tdLNs) were minced and digested with Collagenase D (1
596 mg/mL, Roche) and DNAse I (50 µg/mL, Roche) for 45 minutes at 37°C in a water bath.
597 Digested tissue was then passed through a 70 µm cell strainer and single cells were kept
598 on ice.
599
600 ***Bone marrow derived DCs generation***
601 Bone marrow cells from femurs and tibias were cultured in presence of 20 ng/ml mouse
602 recombinant GM-CSF (Biolegend) for 8 days. Fresh culture medium with cytokine was
603 added on day 3, and on day 6. After harvesting and when indicated, cells were stimulated
604 with 1 ug/mL Tunicamycin (Sigma) for 8h followed by total RNA extraction with Trizol
605 (Invitrogen).
606

607 ***Bone marrow derived cDC1s generation and tumor lysate stimulation***

608 Bone marrow cells from femurs and tibias were cultured in presence of 100 ng/ml
609 recombinant human FLT3-L (Peprotech). After three days of differentiation, cells were
610 plated onto a monolayer of OP9-DL1 stromal cells and co-cultured for additional 6 days
611 in P24 plates as previously reported (38, 39).

612

613 For tumor lysate preparation B78-ChOVA cells were washed twice with PBS, resuspended
614 at $8x10^6$ cells/mL in RPMI supplemented with 10% FBS and aliquoted in cryotubes. Cell
615 suspensions were subjected to heat-shock (42°C for 60 min) followed by three cycles of
616 freeze/thaw (liquid nitrogen/waterbath at 37°C). Tumor lysates were stored at -80°C
617 until use.

618 BM-derived cDC1s were harvested and plated with B78-ChOVA lysates (50 uL/mL) in
619 round-bottom p96 plates. After 14h, Brefeldin A (GolgiPlug, BD) was added and four
620 hours later, cells were harvested and stained for intracellular IL-12p40 expression by
621 flow cytometry.

622

623 ***Xbp1s splicing assay***

624 Total RNA was isolated either by Trizol (Invitrogen) or RNAeasy plus Micro Kit (Qiagen).
625 cDNA was prepared using M-MLV reverse transcriptase (Invitrogen). The following
626 primers were used for conventional PCR amplification of total Xbp1: Fwd: 5'-
627 ACACGCTTGGGAATGGACAC-3' and Rev: 5'-CCATGGGAAGATGTTCTGGG-3' (26); and for
628 beta actin (*Actb*): Fwd: 5'-CTAAGGCCAACCGTGAAAAG-3' and Rev: 5'-
629 TTGCTGATCCACATCTGCTG-3' or alternatively for beta actin (*Actb*): Fwd 5'-
630 GTGACGTTGACATCCGTAAAGA-3' and Rev: 5'-GCCGGACTCATCGTACTCC-3'. PCR
631 products were analyzed on agarose gels.

632

633 ***Flow Cytometry and Cell Sorting***

634 For surface staining, cells were incubated with anti-Fc receptor antibody (anti-CD16/32,
635 Biolegend) and then stained with fluorochrome-conjugated antibodies in FACS buffer
636 (PBS + 1% FBS + 2mM EDTA) for 30 min at 4°C. Viability was assessed by staining with
637 fixable viability Zombie (BioLegend) or LIVE/DEAD fixable (Invitrogen). A biotinylated
638 antibody was used for F4/80 staining, followed by a second staining step with
639 Streptoavidin-APC (Biolegend) for 30 min at 4°C. Flow cytometry was performed on BD
640 Fortessa LSR instrument. Analysis of flow cytometry data was done using FlowJo
641 software. Cell sorting was performed using a BD FACS Aria III.

642

643 ***Transcription Factors and Granzyme B intracellular staining***

644 After surface staining, cells were fixed and permeabilized using Foxp3 transcription factor
645 staining set (eBioscience) followed by intracellular staining of transcription factors
646 (Foxp3, Tcf1, Tox) and/or granzyme B as indicated by the manufacturer protocol.

647

648 ***T cell stimulation and intracellular cytokine staining***

649 Tumor and TdLN cell suspensions were stimulated *ex-vivo* prior to staining with 0.25 μM
650 phorbol 12- myristate 13-acetate (PMA; Sigma) and 1 μg/mL Ionomycin (Sigma) at 37°C
651 and 5% CO_2 for 3.5 hr in the presence of Brefeldin A (BD GolgiPlug). After stimulation,
652 cells were surface stained as mentioned above. Then, cells were fixed and permeabilized
653 using BD Cytofix/Cytoperm fixation/permeabilization kit (BD) followed by intracellular
654 staining of cytokines (IFN-γ, IL-2 and TNF-α) as indicated by the manufacturer protocol.

655

656 ***Tetramer staining***

657 For OVA-specific CD8+ T cell quantification cells were incubated with PE H2-K^b-OVA
658 (SIINFEKL) tetramers (MBL) at room temperature for 30 min protected from light,
659 followed by surface staining and FACS analysis.
660
661 ***t-SNE and clustering***
662 For tSNE visualization of tumor immune infiltrate a multicolor flow cytometry panel was
663 used including 19 parameters (FSC, SSC, Viability, CD45, VenusFP, XCR1, CD4, NK1.1,
664 CD26, F4/80, Ly6G, MHCII, CD24, CD3e, Ly6C, CD8a, CD11c, CD11b, CD19). Cells were
665 compensated for spillover between channels and pre-gated on CD45+ Live singlets using
666 FlowJo. Flowjo workspace was imported into the R environment using CytoML v2.4.0 ,
667 FlowWokspace v4.4.0 and FlowCore v2.4.0 packages (64–66). The intensity values of
668 marker expression were then biexp-transformed via the flowjo_biexp_trans function of
669 FlowWorkspace using parameters ChannelRange=4096, maxValue=262144, pos=4.5,
670 neg=0 and widthBasis=-10. Subsequently 5.000 cell events from each mouse (4 WT and 4
671 ERAI) were randomly sampled and combined for a total of 40.000 single cells. Sampled
672 data was min-max normalized, and subjected to dimensionality reduction by Barnes-
673 Hutts implementation of t-Distributed Stochastic Neighbor Embedding (tSNE) using
674 RtSNE v0.15 package (67). Thirteen parameters were used for tSNE construction (XCR1,
675 CD4, NK1.1, CD26, F4/80, Ly6G, MHCII, CD24, CD3e, Ly6C, CD8a, CD11c, CD11b and CD19)
676 and the parameters were set to iterations=1000 and perplexity =30. After dimensionality
677 reduction, automatic clustering was performed using density based spatial clustering
678 (DBSCAN) using DBSCAN v1.1.8 package (68). Dotplot for marker expression among
679 clusters and Violin plots for VenusFP were then generated using ggplot2 v3.3.5 package
680 (69).
681

682 ***In vivo T cell proliferation assay***

683 LN cells from pmel-1 TCR transgenic mice were isolated and enriched for CD8+ T cells by
684 magnetic negative selection using CD8+ T cell isolation kit (MACS, Miltenyi). Enriched
685 CD8+ T cells were surface stained and naïve CD8+ T cells were purified by cell sorting
686 (CD8a+, CD62L high, CD44low, CD25 neg). After sorting, naïve CD8+ T cells were labeled
687 with Cell Trace Violet (CTV, Invitrogen). $1x10^6$ naïve CD8+ T cells were adoptively
688 transferred into B16-F10 tumor-bearing mice at day 7 after tumor challenge. *In vivo*
689 proliferation and CD44/CD25 expression of transferred T cells was analyzed by FACS in
690 tumor draining lymph nodes 4 days after adoptive transfer.

691

692 ***RNA-seq***

693 Cell suspensions from tumor tissue pooled from 2-4 B16 bearing mice were enriched in
694 immune cells by positive selection with CD45+ biotin magnetic beads (MACS, Miltenyi).
695 Enriched cells were surface stained and 5-20 $x10^3$ intratumoral cDC1s were sorted
696 directly in RLT lysis buffer (Qiagen) containing 2-mercaptoethanol. Immediately after
697 sorting, collected cells were homogenized through vortex and frozen on dry ice before
698 storage at -80°C. Total RNA was extracted with RNAeasy Plus Micro kit (Qiagen). RNA
699 sequencing was performed at VIB Nucleomics Core using SMART-seq v4 pre-
700 amplification followed by single-end sequencing on Illumina NextSeq500. Preprocessing
701 of the RNA-seq data was performed by Trimmomatic v0.39 and quality control by FastQC
702 v0.11.8. Mapping to the reference mouse genome was performed by STAR v2.7.3a and
703 HTSeqCount v0.11.2 was used for counting. Limma v3.42.2 (70) was used to normalize
704 the data. Genes which did not meet the requirement of a count per million (cpm) value
705 larger than 1 in at least 4 samples were filtered. This resulted in an expression table
706 containing 11066 genes. EdgeR v3.28.0 (71) was utilized to perform differential

707 expression analysis. Benjamini-Hochberg correction was used to adjust the p-values for
708 multiple testing. Differentially expressed genes were filtered as genes with a |FC| > 1.5
709 and adjusted p-value < 0.05. Heatmaps were created using pheatmap v1.0.12 package
710 (72) on log2 normalized and mean centered gene expression data.
711
712 ***Gene Set Enrichment Analysis***
713 Over-Representation Analysis (ORA) and Gene Set Enrichment Analysis (GSEA) were
714 performed using *ClusterProfiler* v4.0.5 package (73) in R and Gene Ontology (GO)
715 knowledgebase gene sets. ORA results were considered significant when the q-value was
716 below 0.01. GSEA was performed on pre-ranked mode using as rank metric the signed
717 log10 transformed p-values derived from the differential expression analysis. GSEA was
718 run using the GO:BP database or literature lists of Xbp1-targets and RIDD-targets (47).
719 Results were considered significant when the adjusted p-value was below 0.05.
720
721 **QUANTIFICATION AND STATISTICAL ANALYSIS**
722 No statistical methods were used to predetermine sample size. The experiments were
723 not randomized, and the investigators were not blinded to allocation during
724 experiments and outcome assessment. Statistical analysis was conducted using
725 GraphPad Prism software (v9.1.2). Results are presented as mean ± SEM. Two groups
726 were compared using two tailed t-test for normal distributed data (Shapiro-Wilk test) or
727 using a non-parametric two-tailed Mann-Whitney test as indicated in figure legends.
728 Multiple groups were compared using one-way ANOVA with Tukey post-test. A p-value
729 < 0.05 was considered statistically significant.
730
731 **STUDY APPROVAL**

732 All animal procedures were performed in accordance with institutional guidelines for
733 animal care of the Fundación Ciencia y Vida, the Faculty of Medicine, University of Chile
734 and the VIB, Belgium, and were approved by the local ethics committee.
735
736
737
738
739
740
741
742
743
744
745
746
747
748
749
750

751 ## Author contributions

752 F.F, MR.B, S.J and F.O designed the research; F.F, S.R, S.G, C.F, D.F did the experiments. F.F,
753 S.R, S.J and F.O analyzed the results; C.DN and C.M helped with RNA-seq data analysis;
754 D.Fe provided technical assistance and experimental expertise, T.I and A.L provided
755 critical reagents. F.F. and F.O wrote the manuscript

756

757 ## Acknowledgements

758 We thank Dr Laurie H. Glimcher (Dana-Farber Cancer Institute) for *Xbp1*$^{fl/fl}$ mice; Dr
759 Matthew Krummel (UCSF) for the B78ChOVA cell line; Dr. Juan Carlos Zuñiga-Pflucker
760 (Sunnybrook Research Institute) for the OP9-DL1 cell line; the VIB nucleomics facility for
761 doing the RNA seq experiments and facilities at Universidad de Chile and Fundación
762 Ciencia & Vida. We thank members of the immunology and immunology and cellular
763 stress laboratories for critical support.
764 This work was funded by an International Research Scholar grant from HHMI
765 (HHMI#55008744, FO); FONDECYT grant No 1200793 (FO); FONDECYT grant No
766 1191438 (MR.B); CONICYT/FONDEQUIP/EQM140016; FONDECYT grant No 1212070
767 (AL); ANID grant FB210008 (MR.B and AL); CONICYT-PFCHA/DoctoradoNacional/2017-
768 21170366 (F.F). The work in Belgium was funded by Stichting tegen Kanker (2014/283),
769 FWO-EOS (ID 30837538) and ERC-CoG (ID 819314) (S.J.).

770

771 ## Declaration of interest

772 The authors declare no competing interests.

773

774

775 # FIGURE LEGENDS

776 **Figure 1. cDC1s are predominant cellular targets of IRE1 activation in melanoma**
777 **tumors**.

778 **(A-F)** B16-F10 melanoma cells were implanted intradermally on ERAI or control mice
779 and 11 days after implantation, tumor tissue was analyzed by multicolor flow cytometry.
780 n=4 mice per group, representative of two independent experiments. **(A)** t-SNE of
781 40.000 immune (CD45+) infiltrating cells from melanoma of ERAI or control mice.
782 Colors indicate unsupervised clustering by DBSCAN. **(B)** Marker expression across the
783 different cell clusters identified in (A). See also Supp. Fig 1A. **(C)** t-SNE map colored by
784 VenusFP signal intensity from control or ERAI mice. cDC1 cluster is highlighted in a red
785 circle. **(D)** VenusFP signal quantification across the different cell clusters identified in
786 (A). Median fluorescence intensity for VenusFP is depicted with a "+" inside each violin
787 plot. **(E-F)** Histograms (E) and quantification (F) of VenusFP signal from manually gated
788 immune populations from B16-F10-bearing WT and ERAI mice (see gating strategy in
789 Supp. Fig.2A). Statistical significance is depicted as compact letter display, ANOVA and
790 Tukey post-test between ERAI mice. **(G-H)** Xbp1 splicing assay (G) of tumor cDC1s
791 isolated by cell sorting from B16-FLT3L-bearing WT mice compared to BMDCs treated
792 with 1 μg/mL of the ER-stressor Tunicamycin (Tun) or medium for 8h. (H) Bars show
793 the image quantification of the ratio between Xbp1 spliced (Xbp1s) and total Xbp1
794 (Xbp1s + Xbp1u). n= 3 samples per group (representative of three independent
795 experiments), mean ± s.e.m, ANOVA and Tukey post-test, ** $p<0.01$, *** $p<0.001$. **(I)**
796 Quantification of VenusFP signal from tumor and tumor draining lymph node migratory
797 (mig) and resident (res) cDCs (see gating strategy in Supp. Fig.2B). ** $p<0.01$, ANOVA
798 and Tukey post-test between ERAI mice. n=4 mice per group, representative of two
799 independent experiments, mean ± s.e.m. **(J)** Quantification of VenusFP signal from

800 intratumoral and spleen monocytes (CD11b^{hi} Ly6C^{hi} cells). *** p<0.001, t-test between
801 ERAI mice. n= 3 mice (ERAI) or 1 mouse (WT), representative of two independent
802 experiments, mean ± s.e.m.
803
804 **Figure 2. XBP1 deletion in CD11c-expressing cells results in increased melanoma**
805 **tumor growth**
806 XBP1^{WT} and XBP1$^{\Delta DC}$ mice were implanted with B78ChOVA tumors. **(A)** Tumor growth
807 curves monitored over a period of 12 days. n=19 mice per group. Pooled data from 4
808 independent experiments. **(B)** Tumor size at day 12 post implantation. * p<0.05, two-
809 tailed t-test. n= 51 mice (XBP1^{WT}) or 53 mice (XBP1$^{\Delta DC}$) from animals used throughout
810 this study (pooled data from 12 independent experiments), boxplot. **(C)** Cell counts for
811 tumor immune infiltrate (CD45+). n=31 mice (XBP1^{WT}) or 29 mice (XBP1$^{\Delta DC}$), pooled
812 data from 8 independent experiments, mean ± s.e.m. **(D)** Frequencies of intratumoral
813 cDC subsets. n=5-10, pooled data from two (cDC2) or three (cDC1) independent
814 experiments, mean ± s.e.m. (E) Frequencies of cDC subsets in TdLN. n=4 mice per group,
815 representative of two independent experiments, mean ± s.e.m. **(F-G)** Frequencies of
816 tumor lymphoid and myeloid populations. n=3-12 mice per group, pooled data from two
817 (neutrophils, TAMs, NK) or three (MdCs, T) independent experiments, mean ± s.e.m. **(H)**
818 Tumor Treg (CD3$^+$CD4$^+$Foxp3$^+$), Tconv (CD3$^+$CD4$^+$Foxp3$^-$) and CD8$^+$ T cells (CD3$^+$CD8$^+$)
819 frequencies. n=8 mice per group, pooled data from two independent experiments, mean
820 ± s.e.m.
821
822 **Figure 3. XBP1 deletion in CD11c-expressing cells results in impaired antitumor T**
823 **cell responses and dysbalanced precursor/terminal exhausted T cell ratio.**

824 **(A)** CD40 and PD-L1 expression by tumor cDCs from B78-ChOVA bearing $XBP1^{WT}$ or
825 $XBP1^{\Delta DC}$ mice. n=7 mice per group, pooled data from two independent experiments,
826 mean ± s.e.m. See also TdLN data in Supp. Fig 4A. **(B)** Intracellular IL-12 expression of *in*
827 *vitro* generated cDC1s (FLT3-L/OP9-DL1) upon stimulation with B78-ChOVA lysates.
828 Gated on cDC1s (MHC-II^+ $CD11c^+$ $CD8^+$ $CD11b^-$). *$p < 0.05$, two-tailed Mann-Whitney test.
829 Each dot represents a biological replicate, n=5, data pooled from three independent
830 experiments, mean ± s.e.m. **(C-D)** $Tetramer^+$ CD8+ T cell frequencies in tumor and TdLN
831 from B78-ChOVA bearing $XBP1^{WT}$ or $XBP1^{\Delta DC}$ mice. Gated on $CD3^+CD8^+$ T cells. n=8 mice
832 per group, pooled data from two independent experiments, mean ± s.e.m. **(E-G)**
833 Cytokines expression by tumor $CD8^+$ T cells (E-F) or $CD4^+$ T cells (G) from B78-ChOVA
834 bearing $XBP1^{WT}$ or $XBP1^{\Delta DC}$ mice after ex vivo stimulation with PMA/ION in the
835 presence of BFA. *$p < 0.05$, two-tailed Mann-Whitney test. n=18 mice ($XBP1^{WT}$) or 17
836 mice ($XBP1^{\Delta DC}$), pooled data from 4 independent experiments, mean ± s.e.m. **(H-I)**
837 Precursor exhausted ($PD1^+TCF1^+$ $TIM3^{neg}$) and terminal exhausted ($PD1^+TCF1^{neg}$ $TIM3^+$)
838 $CD8^+$ T cell tumor frequencies from B78-ChOVA bearing $XBP1^{WT}$ or $XBP1^{\Delta DC}$ mice. Gated
839 on $CD3^+CD8^+$ T cells. * $p<0.05$, **$p<0.01$, two-tailed t-test. N=8 mice per group, pooled
840 data from two independent experiments, mean ± s.e.m.
841
842 **Figure 4. Tumor cDC1s from XBP1ΔDC mice display signs of RIDD.**
843 (A) Upon Cre mediated recombination in $XBP1^{fl/fl}$ mice, a premature stop codon is
844 introduced in the *Xbp1* mRNA sequence, preventing the translation of a functional XBP1s
845 protein. XBP1s absence is reported to trigger IRE1 RNase hyperactivation and induce
846 RIDD in certain cell types (26, 36). However, IRE1 RNase activity can still be monitored
847 by determining Xbp1 mRNA splicing ratio. (B) Scheme depicting LoxP sites and IRE1
848 splicing sites at *Xbp1* locus (top) and PCR analysis of Xbp1 splicing in intratumoral

849 cDC1s isolated from B16-bearing XBP1^{WT} and XBP1$^{\Delta DC}$ mice (bottom). Each lane
850 represents different mice. Xbp1u: Xbp1 unspliced; Xbp1s: Xbp1 spliced; Actb: beta actin.
851 (C) CD11c expression by intratumoral cDC1, cDC2 and TAMs from B16-bearing XBP1^{WT}
852 and XBP1$^{\Delta DC}$ mice. Gray histogram depicts unstained control. * $p<0.05$, ** $p<0.01$, ****
853 $p<0.0001$, two-tailed t-test. n=4 mice per group, representative of two independent
854 experiments, mean ± s.e.m. (D) CD11c expression by cDC subsets in the TdLN from B16-
855 bearing XBP1^{WT} and XBP1$^{\Delta DC}$ mice. Gray histogram depicts unstained control. *$p<0.05$,
856 two-tailed Mann-Whitney test. n=4 mice per group, representative of two independent
857 experiments, mean ± s.e.m.
858
859 **Figure 5. Gene expression profiles of tumor cDC1s deficient for IRE1 RNase and**
860 **XBP1.**
861 WT, XBP1$^{\Delta DC}$ and XBP1$^{\Delta DC}$/IRE1^{trunc}DC mice were implanted with B16 tumors. After 12
862 days, tumor cDC1s were isolated by cell sorting and total RNA was sequenced by RNA-
863 seq. **(A)** Heatmap of differentially expressed genes (DEGs). Three groups of genes were
864 identified by the pattern of expression among the three genotypes. **(B)** Over
865 representation analysis of DEGs over the Gene Ontology (GO) database. **(C)** Gene Set
866 Enrichment Analysis (GSEA) of WT vs XBP1$^{\Delta DC}$ cDC1s using GO:Biological Process
867 database. **(D)** GSEA of WT vs XBP1$^{\Delta DC}$/IRE1^{trunc}DC cDC1s using GO:Biological Process
868 database. **(E-F)** GSEA using XBP1s- and RIDD-target gene sets from literature (So et al,
869 2012, Cell Metabolism).
870
871 **Figure 6. RIDD activation in DCs accounts for the changes related to tumor growth**
872 **and dysregulated antitumor T cell immunity noticed in XBP1ΔDC mice.**

873 XBP1^{WT}/IRE1^{WT} and XBP1$^{\Delta DC}$/IRE1^{trunc}DC mice were implanted with B78ChOVA cells.
874 **(A)** Tumor growth curves monitored over a period of 12 days. n=20 mice
875 (XBP1^{WT}/IRE1^{WT}) or 24 mice (XBP1$^{\Delta DC}$/IRE1^{trunc}DC), data pooled from 4 independent
876 experiments. **(B)** Tumor size at day 12 post implantation. n=24 mice (XBP1^{WT}/IRE1^{WT})
877 or 28 mice (XBP1$^{\Delta DC}$/IRE1^{trunc}DC), data pooled from 5 independent experiments, mean ±
878 s.e.m. **(C-D)** Cytokines expression by tumor CD8^{+} T cells after ex vivo stimulation with
879 PMA/Ionomycin in the presence of BFA. Gated on CD3^{+}CD8^{+} T cells. N=9 mice
880 (XBP1^{WT}/IRE1^{WT}) or 11 mice (XBP1$^{\Delta DC}$/IRE1^{trunc}DC), data pooled from three
881 independent experiments, mean ± s.e.m. **(E-F)** Precursor exhausted (PD1^{+}TCF1^{+}
882 TIM3^{neg}) and terminal exhausted (PD1^{+}TCF1^{neg} TIM3^{+}) CD8^{+} T cell tumor frequencies.
883 Gated on CD3^{+}CD8^{+} T cells. n=9 mice (XBP1^{WT}/IRE1^{WT}) or 11 mice
884 (XBP1$^{\Delta DC}$/IRE1^{trunc}DC), data pooled from three independent experiments, mean ± s.e.m.
885

886 # SUPPLEMENTARY FIGURE LEGENDS

887 **Supplementary Figure 1. Immune analysis of melanoma tumors derived from**
888 **ERAI mice.**
889 **(A)** t-SNE map as in figure 1a. Color gradient shows the expression of the indicated
890 marker**. (B)** Quantification of VenusFP signal from manually gated immune populations
891 from MC-38 bearing WT and ERAI mice. **** $p < 0.0001$, ANOVA and Tukey post-test
892 between ERAI mice. n=3 (WT) or 5 (ERAI) mice per group, representative of two
893 independent experiments.(C) Quantification of VenusFP signal of tumor- and spleen-
894 cDC1s from MC-38 bearing WT and ERAI mice. **** $p<0.0001$, t-test between ERAI mice.
895 n=3 (WT) or 5 (ERAI), representative of two independent experiments.
896

897 **Supplementary Figure 2. Gating strategy for tumor associated cDCs.**

898 **(A)** Gating strategy for identification of immune infiltrated populations in tumors.
899 Representative plots from B16 melanoma tumor. **(B)** Gating strategy for identification of
900 migratory (mig) and resident (res) cDC1s and cDC2s in tumor draining lymph node.
901 Representative plots from B16 melanoma TdLN.

902

903 **Supplementary Figure 3. Tumor growth and T cell infiltration in MC-38 bearing**
904 **XBP1$^{\Delta DC}$ mice.**

905 XBP1^{WT} and XBP1$^{\Delta DC}$ mice were implanted with MC-38 tumors. **(A-C)** Tumor volume
906 curves (A), tumor volumes (B) at end point and tumor weight (C) at end point. n=12-13
907 mice per group. Pooled data from two independent experiments.

908

909 **Supplementary Figure 4. Tumor immune cell analysis of XBP1$^{\Delta DC}$ mice.**

910 **(A)** Related to figure 3A. CD40 and PD-L1 expression by TdLN cDCs**.** n=7 mice per group,
911 pooled data from two independent experiments, mean ± s.e.m. **(B)** Related to figure 3B.
912 Dot plots of IL-12 intracellular expression by *in vitro* generated cDC1s stimulated with
913 B78-ChOVA lysates**. (C)** Related to figure 3C-D. Fluorescence minus one (FMO) and
914 tumor-free WT mouse as negative controls for tetramer staining. **(D-E)** XBP1^{WT} and
915 XBP1$^{\Delta DC}$ mice were implanted with B16-F10 tumors. Seven days after implantation,
916 CD8^{+} naïve T cells isolated from pmel1 transgenic mice were labeled with Cell Trace
917 Violet and were adoptively transferred into tumor-bearing mice. Four days later,
918 transferred cell proliferation and CD44/CD25 expression was quantified by FACS. n=8
919 mice (XBP1^{WT}) or 15 mice (XBP1$^{\Delta DC}$), data pooled from two independent experiments,
920 mean ± s.e.m. **(F-G)** CD8+ T cell (F) and CD4+ T cell (G) frequencies and profiles in MC-
921 38 bearing XBP1^{WT} and XBP1$^{\Delta DC}$ mice. n=11-13, pooled data from two independent

922 experiments, mean ± s.e.m. **(H)** Related to figure 3H-I. Representative histograms of
923 different markers associated with terminal exhausted $CD8^+$ T cells. Gated on
924 $CD3^+CD8^+PD1^+TCF1^+$ or $CD3^+CD8^+PD1^+TIM3^+$ as shown in figure 3H.
925

926 **Supplementary Figure 5. IRE1/XBP1s double deficient cDC1s are unable to**
927 **activate RIDD.**

928 **(A)** PCR analysis of Xbp1 splicing in intratumoral cDC1s isolated from B16-bearing
929 $XBP1^{WT}/IRE1^{WT}$ vs $XBP1^{\Delta DC}/IRE1^{trunc}DC$ mice. Each lane represents different mice.
930 Xbp1u: Xbp1 unspliced; Xbp1s: Xbp1 spliced; Actb: beta actin. **(B)** CD11c expression by
931 intratumoral cDC1, cDC2 and TAMs from B16-bearing $XBP1^{WT}/IRE1^{WT}$ vs
932 $XBP1^{\Delta DC}/IRE1^{trunc}DC$ mice. n=4 mice per group, mean ± s.e.m. **(C)** CD11c expression by
933 cDC subsets in the TdLN from B16-bearing $XBP1^{WT}/IRE1^{WT}$ vs $XBP1^{\Delta DC}/IRE1^{trunc}DC$ mice.
934 *$p<0.05$, two-tailed Mann-Whitney test. n=4 mice per group, mean ± s.e.m.
935

936 **Supplementary Figure 6. RNAseq analysis of WT, XBP1 deficient WT vs IRE1/XBP1**
937 **double deficient cDC1s.**

938 **(A)** Heatmap of genes with an adjusted p-value < 0.05 but with a fold change (FC) below
939 the 1.5 threshold. Table summarize log2FC and adj p-values for WT vs XBP1 and WT vs
940 IRE1/XBP1 deficient cDC1s. **(B)** Related to figure 5F-G. GSEA using XBP1s- and RIDD-
941 target gene sets from literature (So et al, 2012, Cell Metabolism). **(C)** GSEA of the
942 "triglyceride biosynthetic process" gene set (GO: 0019432) in WT vs $XBP1^{\Delta DC}$ cDC1s
943 (left) or WT vs $XBP1^{\Delta DC}/IRE1^{trunc}DC$ cDC1s (right) showing not statistically significant
944 enrichment (q-value > 0.05). **(D)** Normalized expression (z-scores) for genes of the
945 "triglyceride biosynthetic process" gene set (GO: 0019432) in WT, $XBP1^{\Delta DC}$, or
946 $XBP1^{\Delta DC}/IRE1^{trunc}DC$ cDC1s.

947 # REFERENCES

948 1. Hildner K et al. Batf3 Deficiency Reveals a Critical Role for CD8 + Dendritic Cells in
949 Cytotoxic T Cell Immunity. *Science* 2008;322(5904):1097–1100.

950 2. Broz ML et al. Dissecting the Tumor Myeloid Compartment Reveals Rare Activating
951 Antigen-Presenting Cells Critical for T Cell Immunity. *Cancer Cell* 2014;26(5):638–652.

952 3. Roberts EW et al. Critical Role for CD103+/CD141+ Dendritic Cells Bearing CCR7 for
953 Tumor Antigen Trafficking and Priming of T Cell Immunity in Melanoma. *Cancer Cell*
954 2016;30(2):324–336.

955 4. Spranger S, Dai D, Horton B, Gajewski TF. Tumor-Residing Batf3 Dendritic Cells Are
956 Required for Effector T Cell Trafficking and Adoptive T Cell Therapy. *Cancer Cell*
957 2017;31(5):711-723.e4.

958 5. Böttcher JP et al. NK Cells Stimulate Recruitment of cDC1 into the Tumor
959 Microenvironment Promoting Cancer Immune Control. *Cell* 2018;172(5):1022-
960 1028.e14.

961 6. Chow MT et al. Intratumoral Activity of the CXCR3 Chemokine System Is Required for
962 the Efficacy of Anti-PD-1 Therapy. *Immunity* 2019;50(6):1498-1512.e5.

963 7. Gerhard GM, Bill R, Messemaker M, Klein AM, Pittet MJ. Tumor-infiltrating dendritic
964 cell states are conserved across solid human cancers. *J. Exp. Med.*
965 2021;218(1):e20200264.

966 8. Schenkel JM et al. Conventional type I dendritic cells maintain a reservoir of
967 proliferative tumor-antigen specific TCF-1+ CD8+ T cells in tumor-draining lymph
968 nodes. *Immunity* 2021;54(10):2338-2353.e6.

969 9. Barry KC et al. A natural killer–dendritic cell axis defines checkpoint therapy–
970 responsive tumor microenvironments. *Nat. Med.* 2018;24(8):1178–1191.

971 10. Sánchez-Paulete AR et al. Cancer immunotherapy with immunomodulatory anti-
972 CD137 and anti–PD-1 monoclonal antibodies requires BATF3-dependent dendritic cells.
973 *Cancer Discov.* 2016;6(1):71–79.

974 11. Salmon H et al. Expansion and Activation of CD103+ Dendritic Cell Progenitors at the
975 Tumor Site Enhances Tumor Responses to Therapeutic PD-L1 and BRAF Inhibition.
976 *Immunity* 2016;44(4):924–938.

977 12. Garris CS et al. Successful Anti-PD-1 Cancer Immunotherapy Requires T Cell-
978 Dendritic Cell Crosstalk Involving the Cytokines IFN-γ and IL-12. *Immunity*
979 2018;49(6):1148-1161.e7.

980 13. Hammerich L et al. Systemic clinical tumor regressions and potentiation of PD1
981 blockade with in situ vaccination. *Nat. Med.* 2019;25(5):814–824.

982 14. Oba T et al. Overcoming primary and acquired resistance to anti-PD-L1 therapy by
983 induction and activation of tumor-residing cDC1s. *Nat. Commun.* 2020;11(1).
984 doi:10.1038/s41467-020-19192-z

985 15. Maier B et al. A conserved dendritic-cell regulatory program limits antitumour
986 immunity. *Nature* 2020;580:256–262.

987 16. Di Pilato M et al. CXCR6 positions cytotoxic T cells to receive critical survival signals
988 in the tumor microenvironment. *Cell* 2021;184(17):4512-4530.e22.

989 17. Binnewies M et al. Unleashing Type-2 Dendritic Cells to Drive Article Unleashing
990 Type-2 Dendritic Cells to Drive Protective Antitumor CD4 + T Cell Immunity. *Cell*
991 2019;177:1–16.

992 18. Walter P, Ron D. The unfolded protein response: From stress pathway to
993 homeostatic regulation. *Science (80-.).* 2011;334(6059):1081–1086.

994 19. Yoshida H, Matsui T, Yamamoto A, Okada T, Mori K. XBP1 mRNA Is Induced by ATF6
995 and Spliced by IRE1 in Response to ER Stress to Produce a Highly Active Transcription
996 Factor2001;107:881–891.

997 20. Calfon M et al. IRE1 couples endoplasmic reticulum load to secretory capacity by
998 processing the XBP-1 mRNA2002;415(January):1–6.

999 21. Hollien J et al. Regulated Ire1-dependent decay of messenger RNAs in mammalian
1000 cells. *J. Cell Biol.* 2009;186(3):323–331.

1001 22. Maurel M, Chevet E, Tavernier J, Gerlo S. Getting RIDD of RNA: IRE1 in cell fate
1002 regulation. *Trends Biochem. Sci.* 2014;39(5):245–254.

1003 23. Wang JM et al. IRE1 prevents hepatic steatosis by processing and promoting the
1004 degradation of select microRNAs. *Sci. Signal.* 2018;11(530):eaao4617.

1005 24. Fink SL et al. IRE1a promotes viral infection by conferring resistance to apoptosis.
1006 *Sci. Signal.* 2017;10(482):eaai7814.

1007 25. Tavernier SJ et al. Regulated IRE1-dependent mRNA decay sets the threshold for
1008 dendritic cell survival. *Nat. Cell Biol.* 2017;19(6):698–710.

1009 26. Osorio F et al. The unfolded-protein-response sensor IRE-1α regulates the function
1010 of CD8α+ dendritic cells. *Nat. Immunol.* 2014;15(3):248–257.

1011 27. Chen X, Cubillos-Ruiz JR. Endoplasmic reticulum stress signals in the tumour and its
1012 microenvironment. *Nat. Rev. Cancer* 2020;21(February):71–88.

1013 28. Song M, Cubillos-ruiz JR. Endoplasmic Reticulum Stress Responses in Intratumoral
1014 Immune Cells : Implications for Cancer Immunotherapy. *Trends Immunol.*
1015 2019;40(2):128–141.

1016 29. Guilliams M et al. Unsupervised High-Dimensional Analysis Aligns Dendritic Cells
1017 across Tissues and Species. *Immunity* 2016;45(3):669–684.

1018 30. Cubillos-Ruiz JR et al. ER Stress Sensor XBP1 Controls Anti-tumor Immunity by
1019 Disrupting Dendritic Cell Homeostasis. *Cell* 2015;161(7):1527–1538.

1020 31. Dong H et al. The IRE1 endoplasmic reticulum stress sensor activates natural killer
1021 cell immunity in part by regulating c-Myc. *Nat. Immunol.* 2019;20(7):865–878.

1022 32. Song M et al. IRE1α–XBP1 controls T cell function in ovarian cancer by regulating
1023 mitochondrial activity. *Nature* 2018;562(7727):423–428.

1024 33. Iwawaki T, Akai R, Kohno K, Miura M. A transgenic mouse model for monitoring
1025 endoplasmic reticulum stress. *Nat. Med.* 2004;10(1):98–102.

1026 34. Mach N et al. Differences in dendritic cells stimulated in vivo by tumors engineered
1027 to secrete granulocyte-macrophage colony-stimulating factor or Flt3-ligand. *Cancer Res.*
1028 2000;60(12):3239–3246.

1029 35. Ruhland MK et al. Visualizing Synaptic Transfer of Tumor Antigens among Dendritic
1030 Cells. *Cancer Cell* 2020;37(6):786-799.e5.

1031 36. Lee A, Scapa E, Cohen D, Glimcher L. Regulation of hepatic lipogenesis by the
1032 transcription factor XBP1. *Science* 2008;320(5882):1492–1496.

1033 37. Caton ML, Smith-Raska MR, Reizis B. Notch–RBP-J signaling controls the homeostasis
1034 of CD8 ⁻ dendritic cells in the spleen. *J. Exp. Med.* 2007;204(7):1653–1664.

1035 38. Cells CCD et al. Notch Signaling Facilitates In Vitro Generation of Resource Notch
1036 Signaling Facilitates In Vitro Generation of Cross-Presenting Classical Dendritic
1037 Cells2018;3658–3672.

1038 39. Balan S et al. Large-Scale Human Dendritic Cell Differentiation Revealing Notch-
1039 Dependent Lineage Bifurcation and Heterogeneity. *Cell Rep.* 2018;24(7):1902-1915.e6.

1040 40. Overwijk WW et al. Tumor Regression and Autoimmunity after Reversal of a
1041 Functionally Tolerant State of Self-reactive CD8 ⁺ T Cells. *J. Exp. Med.* 2003;198(4):569–
1042 580.

1043 41. Miller BC et al. Subsets of exhausted CD8+ T cells differentially mediate tumor
1044 control and respond to checkpoint blockade. *Nat. Immunol.* 2019;20(3):326–336.

1045 42. Philip M, Schietinger A. CD8+ T cell differentiation and dysfunction in cancer. *Nat.*
1046 *Rev. Immunol.* 2021;Online ahead of print.

1047 43. Chen Z et al. TCF-1-Centered Transcriptional Network Drives an Effector versus
1048 Exhausted CD8 T Cell-Fate Decision. *Immunity* 2019;51(5):840-855.e5.

1049 44. Sade-Feldman M et al. Defining T Cell States Associated with Response to Checkpoint
1050 Immunotherapy in Melanoma. *Cell* 2018;175(4):998-1013.e20.

1051 45. Iwawaki T, Akai R, Yamanaka S, Kohno K. Function of IRE1 alpha in the placenta is
1052 essential for placental development and embryonic viability. *Proc. Natl. Acad. Sci. U. S. A.*
1053 2009;106(39):16657–16662.

1054 46. Lee AS. The ER chaperone and signaling regulator GRP78/BiP as a monitor of
1055 endoplasmic reticulum stress. *Methods* 2005;35(4):373–381.

1056 47. So JS et al. Silencing of lipid metabolism genes through ire1α-mediated Mrna decay
1057 lowers plasma lipids in mice. *Cell Metab.* 2012;16(4):487–499.

1058 48. Janssens S, Pulendran B, Lambrecht BN. Emerging functions of the unfolded protein
1059 response in immunity. *Nat. Immunol.* 2014;15(10):910–919.

1060 49. Grootjans J, Kaser A, Kaufman RJ, Blumberg RS. The unfolded protein response in
1061 immunity and inflammation. *Nat. Rev. Immunol.* 2016;16(8):469–484.

1062 50. Shaffer AL et al. XBP1, downstream of Blimp-1, expands the secretory apparatus and
1063 other organelles, and increases protein synthesis in plasma cell differentiation.
1064 *Immunity* 2004;21(1):81–93.

1065 51. Bettigole SE et al. The transcription factor XBP1 is selectively required for eosinophil
1066 differentiation. *Nat. Immunol.* 2015;16(8):829–837.

1067 52. Batista A et al. IRE1α regulates macrophage polarization, PD-L1 expression, and
1068 tumor survival. *PLoS Biol.* 2020;18(6):1–26.

1069 53. Scarlett UK et al. Ovarian cancer progression is controlled by phenotypic changes in
1070 dendritic cells. *J. Exp. Med.* 2012;209(3):495–506.

1071 54. Huarte E et al. Depletion of dendritic cells delays ovarian cancer progression by
1072 boosting antitumor immunity. *Cancer Res.* 2008;68(18):7684–7691.

1073 55. Fuertes MB et al. Host type I IFN signals are required for antitumor CD8 + T cell
1074 responses through CD8α + dendritic cells. *J. Exp. Med.* 2011;208(10):2005–2016.

1075 56. Ferris ST et al. cDC1 prime and are licensed by CD4+ T cells to induce anti-tumour
1076 immunity. *Nature* 2020;584(7822):624–629.

1077 57. Duong E et al. Type I interferon activates MHC class I-dressed CD11b+ conventional
1078 dendritic cells to promote protective anti-tumor CD8+ T cell immunity. *Immunity*
1079 2022;55(2):308-323.e9.

1080 58. MacNabb BW et al. Dendritic cells can prime anti-tumor CD8+ T cell responses
1081 through major histocompatibility complex cross-dressing. *Immunity* 2022;55(6):982-
1082 997.e8.

1083 59. Theisen DJ et al. Batf3-dependent genes control tumor rejection induced by dendritic
1084 cells independently of cross-presentation. *Cancer Immunol. Res.* 2019;7(1):29–39.

1085 60. Marciniak SJ, Chambers JE, Ron D. Pharmacological targeting of endoplasmic
1086 reticulum stress in disease. *Nat. Rev. Drug Discov.* 2022;21(2):115–140.

1087 61. Guttman O et al. Antigen-derived peptides engage the ER stress sensor IRE1α to curb
1088 dendritic cell cross-presentation. *J. Cell Biol.* 2022;221(6). doi:10.1083/jcb.202111068

1089 62. Guo-Ping S et al. Cathepsin S required for normal MHC class II peptide loading and
1090 germinal center development. *Immunity* 1999;10(2):197–206.

1091 63. Schmitt TM, Zúñiga-Pflücker JC. Induction of T cell development from hematopoietic
1092 progenitor cells by delta-like-1 in vitro. *Immunity* 2002;17(6):749–756.

1093 64. Finak G, Jiang W, Gottardo R. CytoML for cross-platform cytometry data sharing.
1094 *Cytom. Part A* 2018;93(12):1189–1196.

1095 65. Ellis B et al. flowCore: flowCore: Basic structures for flow cytometry data2021;

1096 66. Finak G, Jiang M. flowWorkspace: Infrastructure for representing and interacting
1097 with gated and ungated cytometry data sets2021;

1098 67. Krijthe JH. Rtsne: T-Distributed Stochastic Neighbor Embedding using a Barnes-Hut
1099 Implementation2015;

1100 68. Hahsler M, Piekenbrock M, Doran D. Dbscan: Fast density-based clustering with R. *J.*
1101 *Stat. Softw.* 2019;91(1). doi:10.18637/jss.v091.i01

1102 69. Wickham H. *ggplot2: Elegant Graphics for Data Analysis*. Springer-Verlag New York;
1103 2016:

1104 70. Ritchie ME et al. Limma powers differential expression analyses for RNA-sequencing
1105 and microarray studies. *Nucleic Acids Res.* 2015;43(7):e47.

1106 71. Robinson M, McCarthy D, Smyth G. edgeR: a Bioconductor package for differential
1107 expression analysis of digital gene expression data. *Bioinformatics* 2010;26:139–140.

1108 72. Kolde R. pheatmap: Pretty Heatmaps2019;

1109 73. Wu T et al. clusterProfiler 4.0: A universal enrichment tool for interpreting omics
1110 data. *Innov.* 2021;2(3):100141.

1111

Figure 1

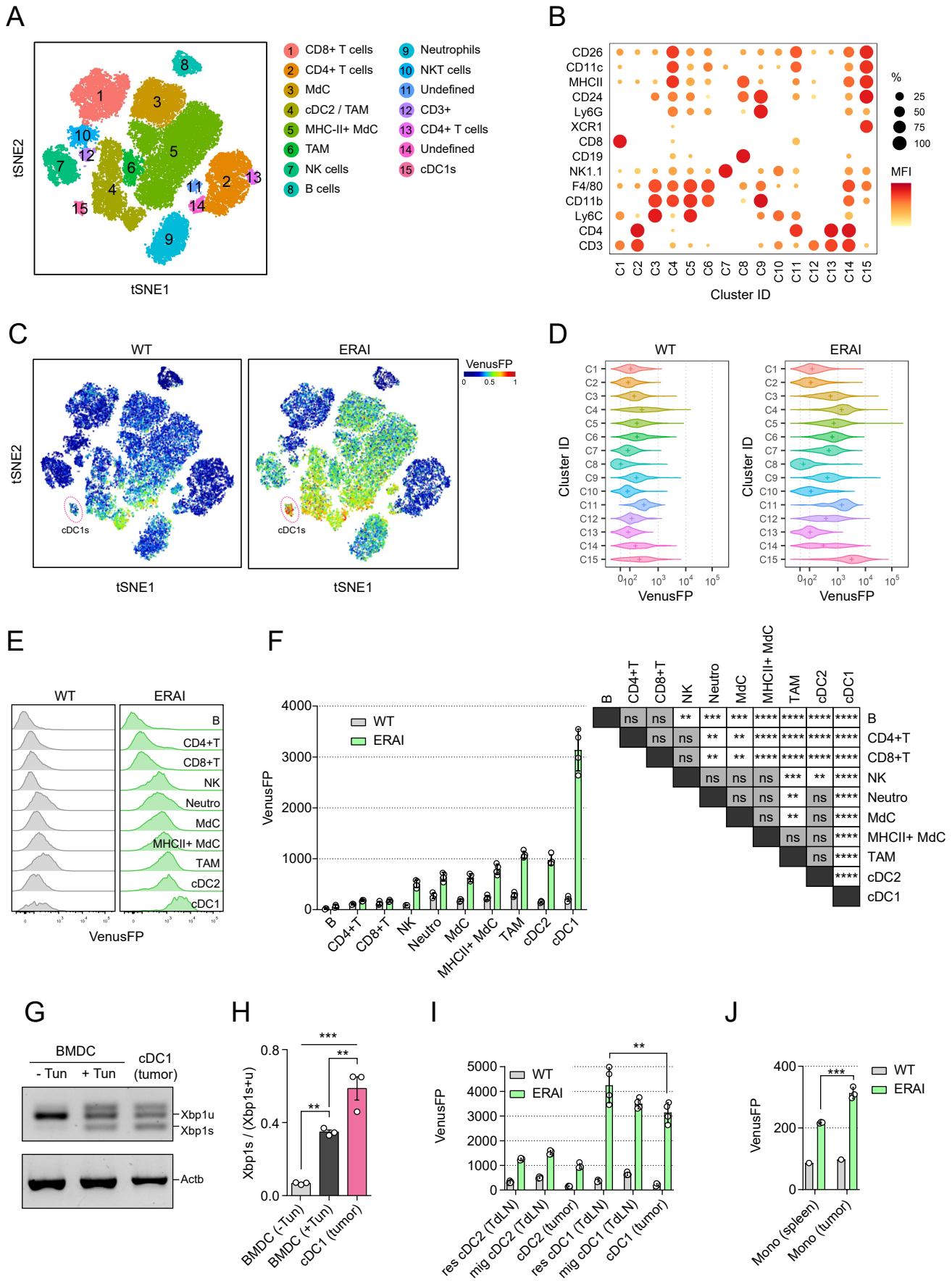
A
tSNE2
tSNE1
1 CD8+ T cells
2 CD4+ T cells
3 MdC
4 cDC2 / TAM
5 MHC-II+ MdC
6 TAM
7 NK cells
8 B cells
9 Neutrophils
10 NKT cells
11 Undefined
12 CD3+
13 CD4+ T cells
14 Undefined
15 cDC1s
B
CD26
CD11c
MHCII
CD24
Ly6G
XCR1
CD8
CD19
NK1.1
F4/80
CD11b
Ly6C
CD4
CD3
Cluster ID
%
25
50
75
100
MFI
C
WT
ERAI
VenusFP
cDC1s
D
Cluster ID
VenusFP
E
WT
ERAI
B
CD4+T
CD8+T
NK
Neutro
MdC
MHCII+ MdC
TAM
cDC2
cDC1
F
WT
ERAI
VenusFP
G
BMDC
- Tun
+ Tun
cDC1 (tumor)
Xbp1u
Xbp1s
Actb
H
Xbp1s / (Xbp1s+u)
BMDC (-Tun)
BMDC (+Tun)
cDC1 (tumor)
I
res cDC2 (TdLN)
mig cDC2 (TdLN)
cDC2 (tumor)
res cDC1 (TdLN)
mig cDC1 (TdLN)
cDC1 (tumor)
J
Mono (spleen)
Mono (tumor)

Figure 2

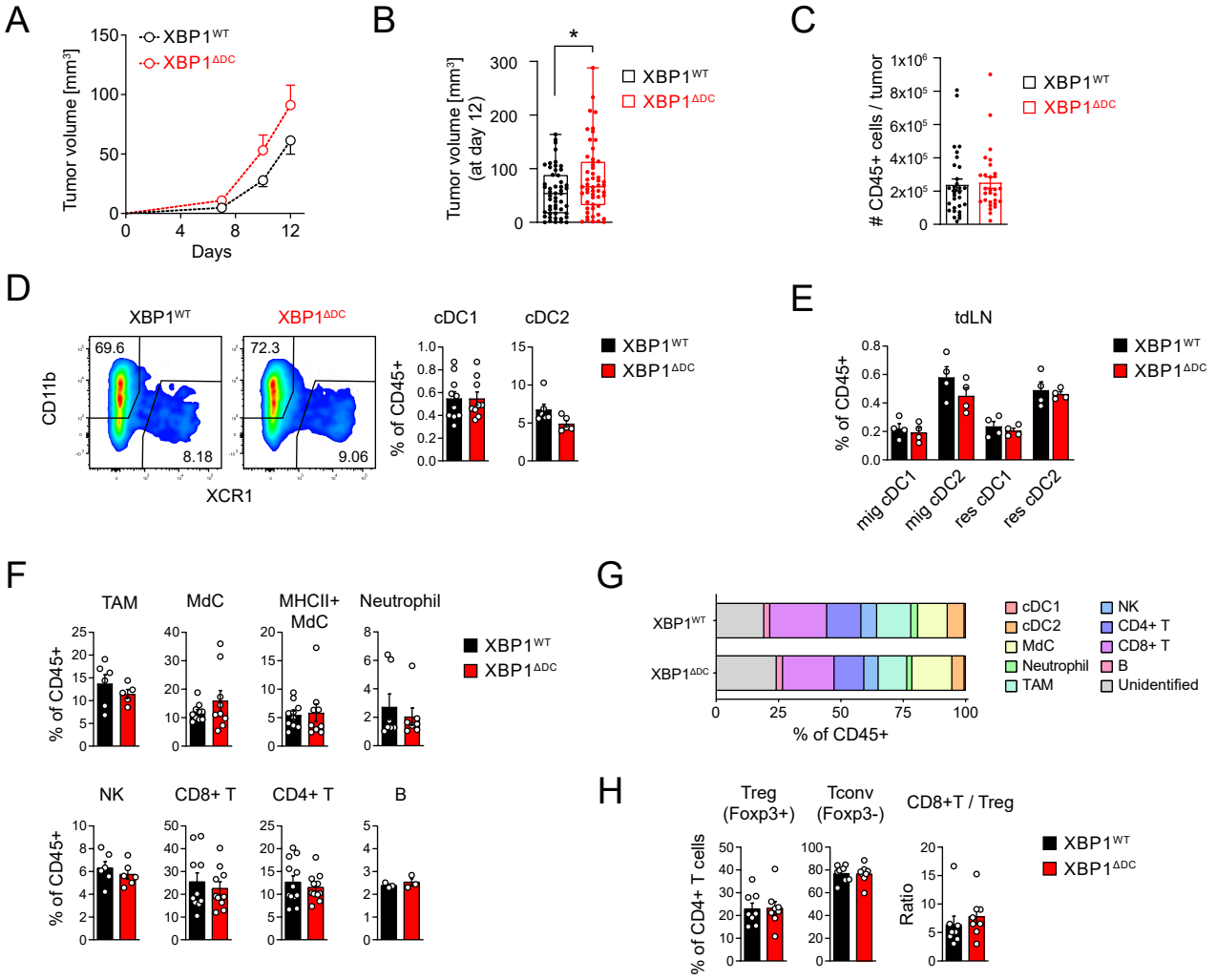
A
XBP1WT
XBP1ΔDC
Tumor volume [mm3]
Days
B
Tumor volume [mm3] (at day 12)
*
C
CD45+ cells / tumor
D
XBP1WT
XBP1ΔDC
CD11b
XCR1
69.6
8.18
72.3
9.06
cDC1
cDC2
% of CD45+
E
tdLN
mig cDC1
mig cDC2
res cDC1
res cDC2
F
TAM
MdC
MHCII+ MdC
Neutrophil
NK
CD8+ T
CD4+ T
B
G
% of CD45+
cDC1
cDC2
MdC
Neutrophil
TAM
NK
CD4+ T
CD8+ T
B
Unidentified
H
Treg (Foxp3+)
Tconv (Foxp3-)
CD8+T / Treg
% of CD4+ T cells
Ratio

Figure 3

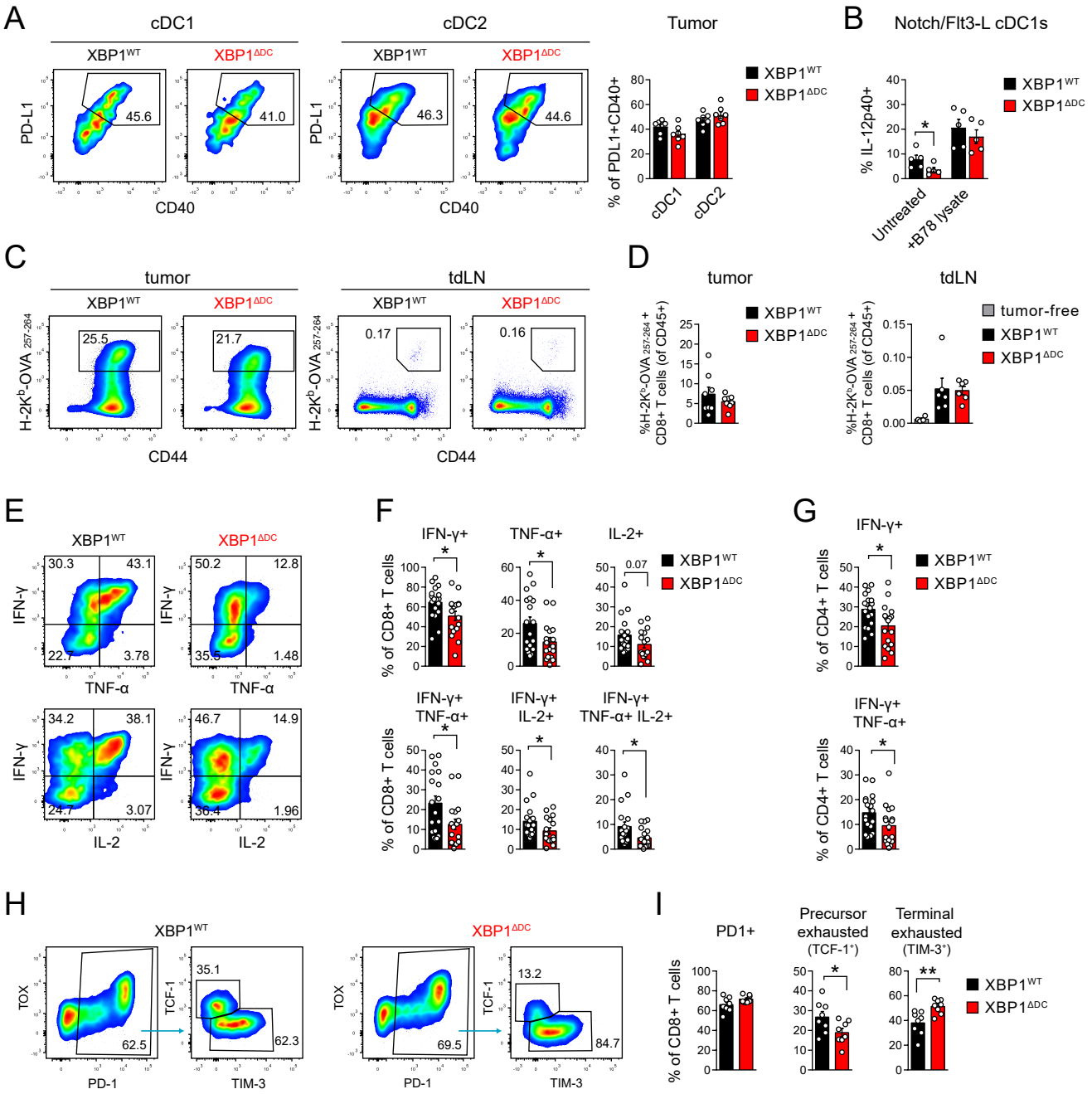
A
cDC1
cDC2
Tumor
XBP1WT
XBP1ΔDC
PD-L1
CD40
45.6
41.0
46.3
44.6
% of PDL1+CD40+
B
Notch/Flt3-L cDC1s
% IL-12p40+
Untreated
+B78 lysate
C
tumor
tdLN
H-2Kb-OVA 257-264
CD44
25.5
21.7
0.17
0.16
D
%H-2Kb-OVA 257-264 + CD8+ T cells (of CD45+)
tumor-free
E
IFN-γ
TNF-α
IL-2
30.3
43.1
22.7
3.78
50.2
12.8
35.5
1.48
34.2
38.1
24.7
3.07
46.7
14.9
36.4
1.96
F
IFN-γ+
TNF-α+
IL-2+
IFN-γ+ TNF-α+
IFN-γ+ IL-2+
IFN-γ+ TNF-α+ IL-2+
% of CD8+ T cells
0.07
G
% of CD4+ T cells
H
TOX
TCF-1
PD-1
TIM-3
62.5
35.1
62.3
69.5
13.2
84.7
I
PD1+
Precursor exhausted (TCF-1+)
Terminal exhausted (TIM-3+)

Figure 4

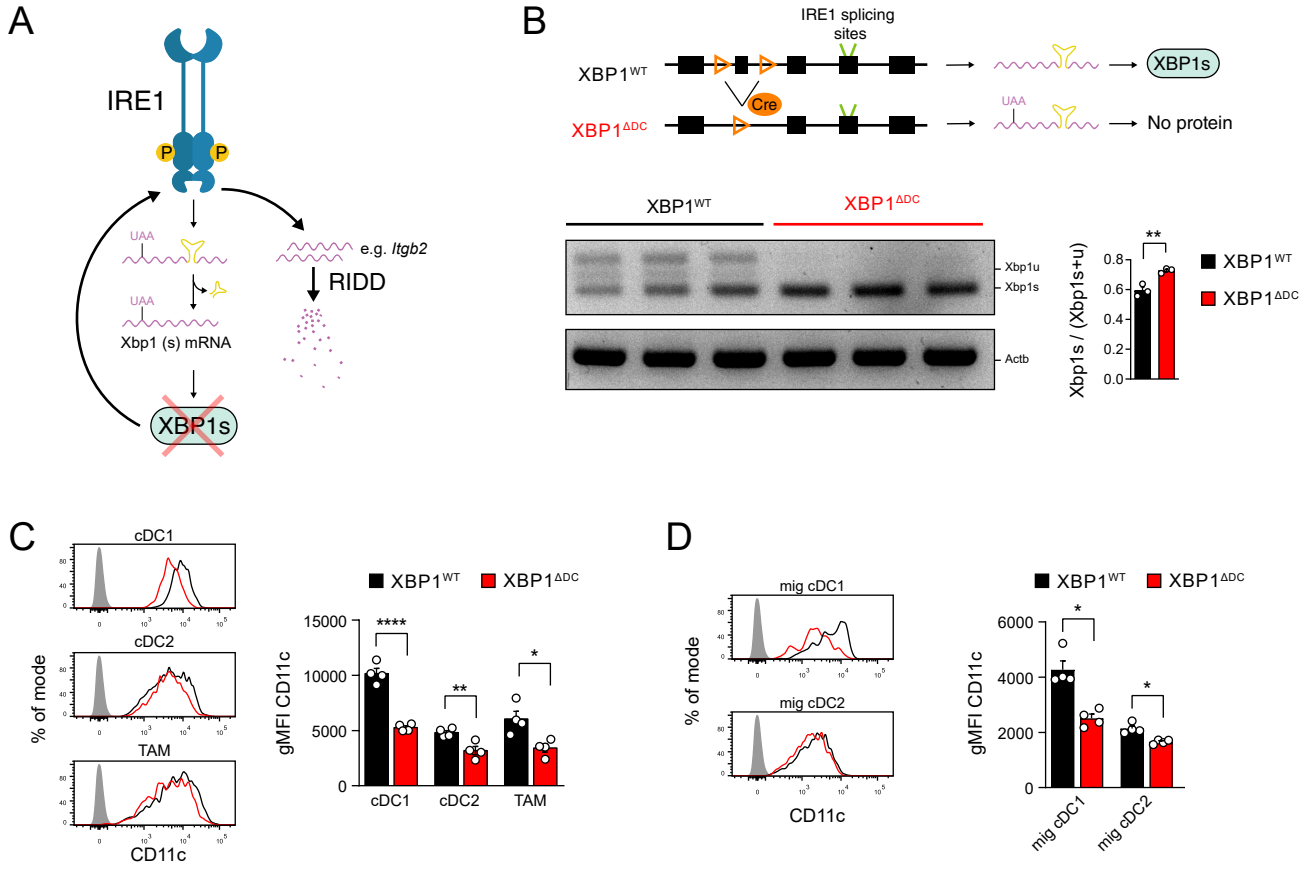
A
IRE1
P
P
UAA
UAA
Xbp1 (s) mRNA
XBP1s
e.g. Itgb2
RIDD
B
IRE1 splicing sites
XBP1WT
Cre
XBP1ΔDC
UAA
XBP1s
No protein
XBP1WT
XBP1ΔDC
Xbp1u
Xbp1s
Actb
Xbp1s / (Xbp1s+u)
0.8
0.6
0.4
0.2
0.0
**
XBP1WT
XBP1ΔDC
C
cDC1
cDC2
TAM
% of mode
CD11c
XBP1WT
XBP1ΔDC
gMFI CD11c
15000
10000
5000
0
****
**
*
cDC1
cDC2
TAM
D
mig cDC1
mig cDC2
% of mode
CD11c
XBP1WT
XBP1ΔDC
gMFI CD11c
6000
4000
2000
0
*
*
mig cDC1
mig cDC2

Figure 5

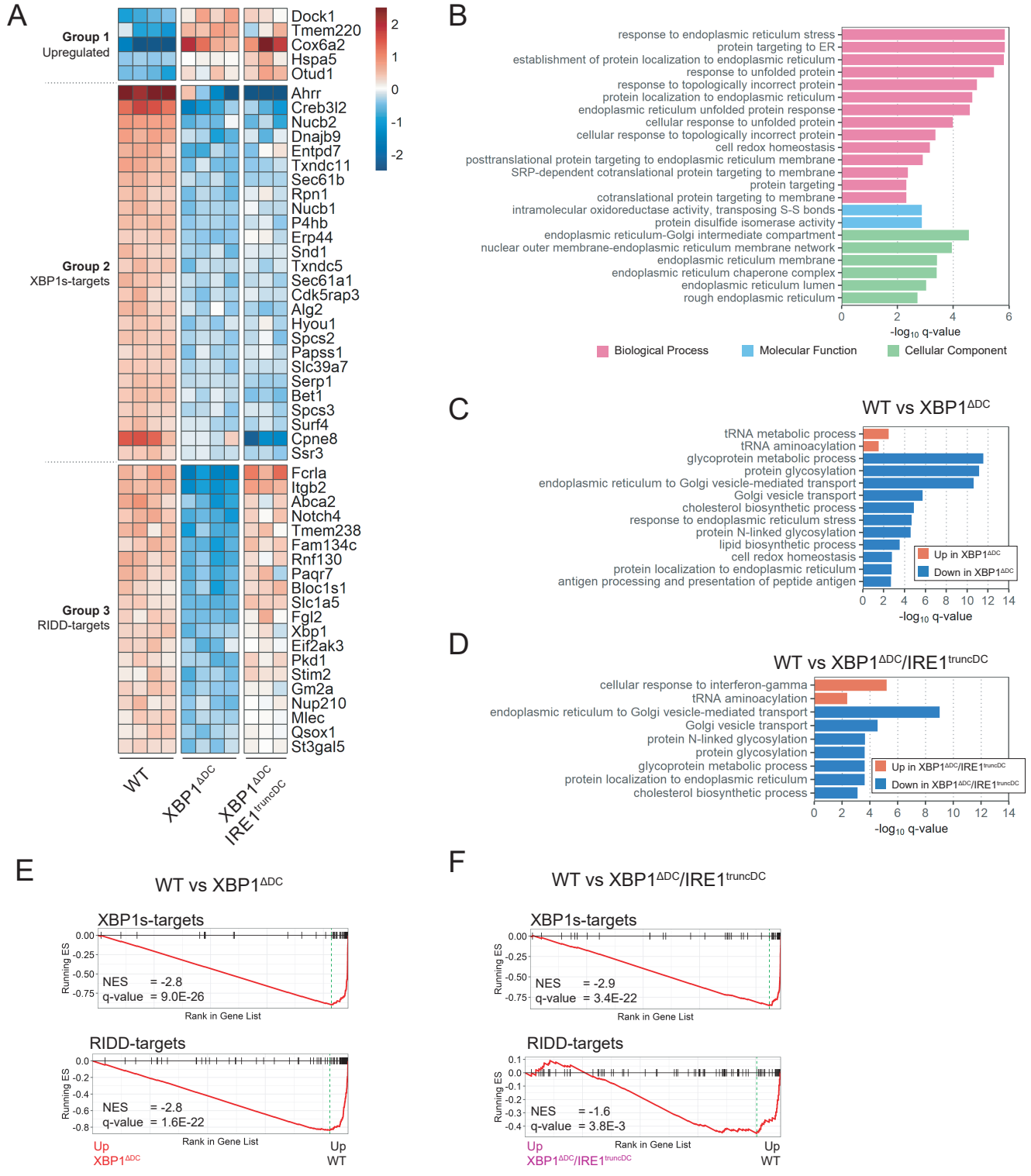
A
Group 1
Upregulated
Dock1
Tmem220
Cox6a2
Hspa5
Otud1
Group 2
XBP1s-targets
Ahrr
Creb3l2
Nucb2
Dnajb9
Entpd7
Txndc11
Sec61b
Rpn1
Nucb1
P4hb
Erp44
Snd1
Txndc5
Sec61a1
Cdk5rap3
Alg2
Hyou1
Spcs2
Papss1
Slc39a7
Serp1
Bet1
Spcs3
Surf4
Cpne8
Ssr3
Group 3
RIDD-targets
Fcrla
Itgb2
Abca2
Notch4
Tmem238
Fam134c
Rnf130
Paqr7
Bloc1s1
Slc1a5
Fgl2
Xbp1
Eif2ak3
Pkd1
Stim2
Gm2a
Nup210
Mlec
Qsox1
St3gal5
2
1
0
-1
-2
WT
XBP1ΔDC
XBP1ΔDC IRE1truncDC
B
response to endoplasmic reticulum stress
protein targeting to ER
establishment of protein localization to endoplasmic reticulum
response to unfolded protein
response to topologically incorrect protein
protein localization to endoplasmic reticulum
endoplasmic reticulum unfolded protein response
cellular response to unfolded protein
cellular response to topologically incorrect protein
cell redox homeostasis
posttranslational protein targeting to endoplasmic reticulum membrane
SRP-dependent cotranslational protein targeting to membrane
protein targeting
cotranslational protein targeting to membrane
intramolecular oxidoreductase activity, transposing S-S bonds
protein disulfide isomerase activity
endoplasmic reticulum-Golgi intermediate compartment
nuclear outer membrane-endoplasmic reticulum membrane network
endoplasmic reticulum membrane
endoplasmic reticulum chaperone complex
endoplasmic reticulum lumen
rough endoplasmic reticulum
0
2
4
6
-log10 q-value
Biological Process
Molecular Function
Cellular Component
C
WT vs XBP1ΔDC
tRNA metabolic process
tRNA aminoacylation
glycoprotein metabolic process
protein glycosylation
endoplasmic reticulum to Golgi vesicle-mediated transport
Golgi vesicle transport
cholesterol biosynthetic process
response to endoplasmic reticulum stress
protein N-linked glycosylation
lipid biosynthetic process
cell redox homeostasis
protein localization to endoplasmic reticulum
antigen processing and presentation of peptide antigen
Up in XBP1ΔDC
Down in XBP1ΔDC
0 2 4 6 8 10 12 14
-log10 q-value
D
WT vs XBP1ΔDC/IRE1truncDC
cellular response to interferon-gamma
tRNA aminoacylation
endoplasmic reticulum to Golgi vesicle-mediated transport
Golgi vesicle transport
protein N-linked glycosylation
protein glycosylation
glycoprotein metabolic process
protein localization to endoplasmic reticulum
cholesterol biosynthetic process
Up in XBP1ΔDC/IRE1truncDC
Down in XBP1ΔDC/IRE1truncDC
0 2 4 6 8 10 12 14
-log10 q-value
E
WT vs XBP1ΔDC
XBP1s-targets
Running ES
0.00
-0.25
-0.50
-0.75
NES = -2.8
q-value = 9.0E-26
Rank in Gene List
RIDD-targets
0.0
-0.2
-0.4
-0.6
-0.8
NES = -2.8
q-value = 1.6E-22
Up XBP1ΔDC
Rank in Gene List
Up WT
F
WT vs XBP1ΔDC/IRE1truncDC
XBP1s-targets
Running ES
0.00
-0.25
-0.50
-0.75
NES = -2.9
q-value = 3.4E-22
Rank in Gene List
RIDD-targets
0.1
0.0
-0.1
-0.2
-0.3
-0.4
NES = -1.6
q-value = 3.8E-3
Up XBP1ΔDC/IRE1truncDC
Rank in Gene List
Up WT

Figure 6

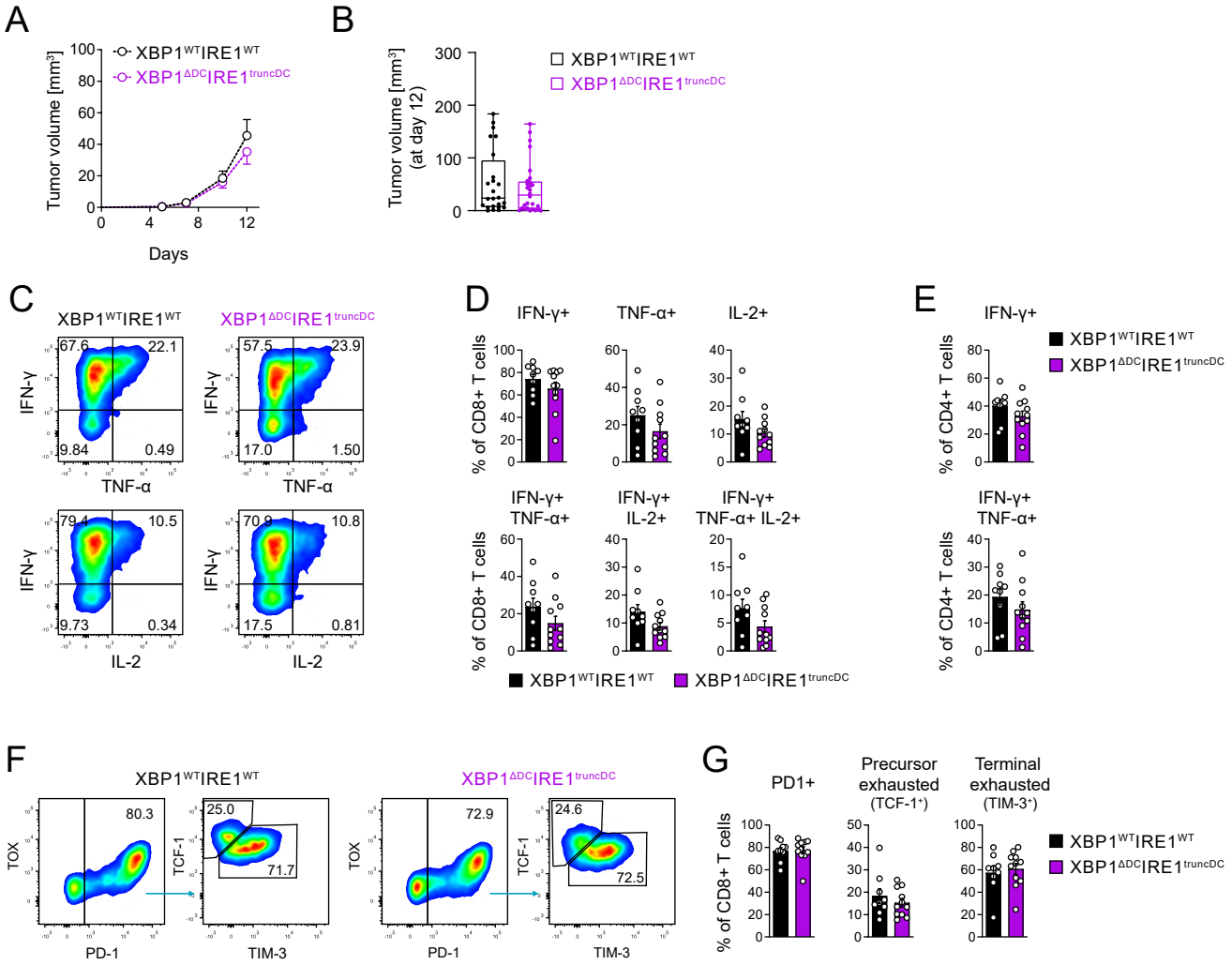
A
Tumor volume [mm³]
XBP1WTIRE1WT
XBP1ΔDCIRE1truncDC
Days
B
Tumor volume [mm³] (at day 12)
C
IFN-γ
TNF-α
IL-2
67.6
22.1
9.84
0.49
57.5
23.9
17.0
1.50
79.4
10.5
9.73
0.34
70.9
10.8
17.5
0.81
D
IFN-γ+
TNF-α+
IL-2+
IFN-γ+ TNF-α+
IFN-γ+ IL-2+
IFN-γ+ TNF-α+ IL-2+
% of CD8+ T cells
E
% of CD4+ T cells
F
TOX
TCF-1
PD-1
TIM-3
80.3
25.0
71.7
72.9
24.6
72.5
G
PD1+
Precursor exhausted (TCF-1+)
Terminal exhausted (TIM-3+)